

zELDA II: reconstruction of galactic Lyman-alpha spectra attenuated by the intergalactic medium using neural networks

Siddhartha Gurung-López^{1,2*}, Chris Byrohl³, Max Gronke⁴, Daniele Spinoso⁵, Alberto Torralba^{1,2}, Alberto Fernández-Soto⁷, Pablo Arnalte-Mur^{1,2}, and Vicent J. Martínez^{1,2,6}

¹ Observatori Astronòmic de la Universitat de València, Ed. Instituts d'Investigació, Parc Científic. C/ Catedrático José Beltrán, n2, 46980 Paterna, Valencia, Spain

² Departament d'Astronomia i Astrofísica, Universitat de València, 46100 Burjassot, Spain

³ Universität Heidelberg, Institut für Theoretische Astrophysik, ZAH, Albert-Ueberle-Str. 2, 69120 Heidelberg, Germany

⁴ Max Planck Institute for Astrophysics, Karl-Schwarzschild-Str. 1, 85748 Garching, Germany

⁵ Department of Astronomy, Physics Building, Tsinghua University, 100084 Beijing, China

⁶ Unidad Asociada "Grupo de Astrofísica Extragaláctica y Cosmología", IFCA-CSIC/Universitat de València, València, Spain

⁷ Instituto de Física de Cantabria (CSIC-UC), Avda. Los Castros s/n, 39005 Santander, Spain

Received ???; accepted ???

ABSTRACT

Context. The observed Lyman-Alpha ($\text{Ly}\alpha$) line profile is a convolution of the complex $\text{Ly}\alpha$ radiative transfer taking place in the interstellar, circumgalactic and intergalactic medium (ISM, CGM, and IGM, respectively). Discerning the different components of the $\text{Ly}\alpha$ line is crucial in order to use it as a probe of galaxy formation or the evolution of the IGM.

Aims. We present the second version of zELDA (redshift Estimator for Line profiles of Distant Lyman-Alpha emitters), an open-source Python module focused on modeling and fitting observed $\text{Ly}\alpha$ line profiles. This new version of zELDA focuses on disentangling the galactic from the IGM effects.

Methods. We build realistic $\text{Ly}\alpha$ line profiles that include the ISM and IGM contributions, by combining the Monte Carlo radiative transfer simulations for the so called 'shell model' (ISM) and IGM transmission curves generated from IllustrisTNG100. We use these mock line profiles to train different artificial neural networks. These use as input the observed spectrum and output the outflow parameters of the best fitting 'shell model' along with the redshift and $\text{Ly}\alpha$ emission IGM escape fraction of the source.

Results. We measure the accuracy of zELDA on mock $\text{Ly}\alpha$ line profiles. We find that zELDA is capable of reconstructing the ISM emerging $\text{Ly}\alpha$ line profile with high accuracy (Kolmogórov-Smirnov < 0.1) for 95% of the cases for HST/COS-like observations and 80% for MUSE-WIDE-like. zELDA is able to measure the IGM transmission with the typical uncertainties below 10% for HST/COS and MUSE-WIDE data.

Conclusions. This work represents a step forward in the high-precision reconstruction of IGM attenuated $\text{Ly}\alpha$ line profiles. zELDA allows the disentanglement of the galactic and IGM contribution shaping the $\text{Ly}\alpha$ line shape, and thus allows us to use $\text{Ly}\alpha$ as a tool to study galaxy and ISM evolution.

Key words. Radiative transfer, Galaxies: intergalactic medium, Galaxies: ISM

1. Introduction

Due to the large abundance of hydrogen in the Universe, the Lyman- α ($\text{Ly}\alpha$) emission line is of imperious importance in astrophysics. $\text{Ly}\alpha$ photons are produced when an electron decays from the first excited level to the ground energy level in hydrogen. The $\text{Ly}\alpha$ line is very luminous in extragalactic sources and thus, is used to identify galaxies throughout the evolution of the Universe (for a review, see, Ouchi et al. 2020).

In the recent years many experiments have expanded the number of known $\text{Ly}\alpha$ emitting galaxies (LAEs), such as HETDEX (~ 0.8 million $\text{Ly}\alpha$ emitting galaxies at $1.9 < z < 3.5$; Hill et al. 2008; Farrow et al. 2021; Weiss et al. 2021), SILVER-RUSH ($\sim 2,000$ at $6 < z < 7$; Ouchi et al. 2018; Kakuma et al. 2019), MUSE WIDE (~ 500 at $3 \leq z \leq 6$; Herenz et al. 2017; Urrutia et al. 2019; Caruana et al. 2020) or the J-PLUS ($\sim 14,500$ at $2 \leq z \leq 3.3$; Spinoso et al. 2020), 67 at $2 < z < 3.75$ in miniJPAS/J-NEP (Torralba-Torregrosa et al. 2023) and in PAUS

(591 at $2.7 < z < 5.3$ Torralba-Torregrosa et al. 2024). Meanwhile, *The Prime Focus Spectrograph Galaxy Evolution Survey* (Greene et al. 2022) will increase our knowledge about LAEs from $z \sim 2$ up to the epoch of reionization at $z \sim 7$.

The $\text{Ly}\alpha$ line constitutes a unique tracer of the composition and kinematics of cold gas. This is because of the resonant nature of $\text{Ly}\alpha$, which implies that $\text{Ly}\alpha$ photons are absorbed and re-emitted by neutral hydrogen atoms in a short time scale ($\sim 10^{-8}$ s). $\text{Ly}\alpha$ emitting galaxies typically exhibit a hydrogen column density is $N_{\text{HI}} \sim 10^{17} - 10^{20} \text{ cm}^{-2}$ (Gronke et al. 2016), and the scattering cross section at the center of the line is $\sigma \sim 6 \times 10^{-14} \text{ cm}^2$ (assuming gas at $T \sim 10^4$ K). This causes the $\text{Ly}\alpha$ photons to experience thousands of scattering events before leaving the galaxy, in which the frequency of the photon changes, mostly due to Doppler boosting. In general, this modifies the shape of the $\text{Ly}\alpha$ line profile emerging from the interstellar medium.

The $\text{Ly}\alpha$ photons furthermore interact on larger scales after leaving their emitting galaxy. In the circumgalactic medium (CGM), the diffuse gas bound to the galaxy's hosting halo, and

* E-mail: gurung.lopez@gmail.com

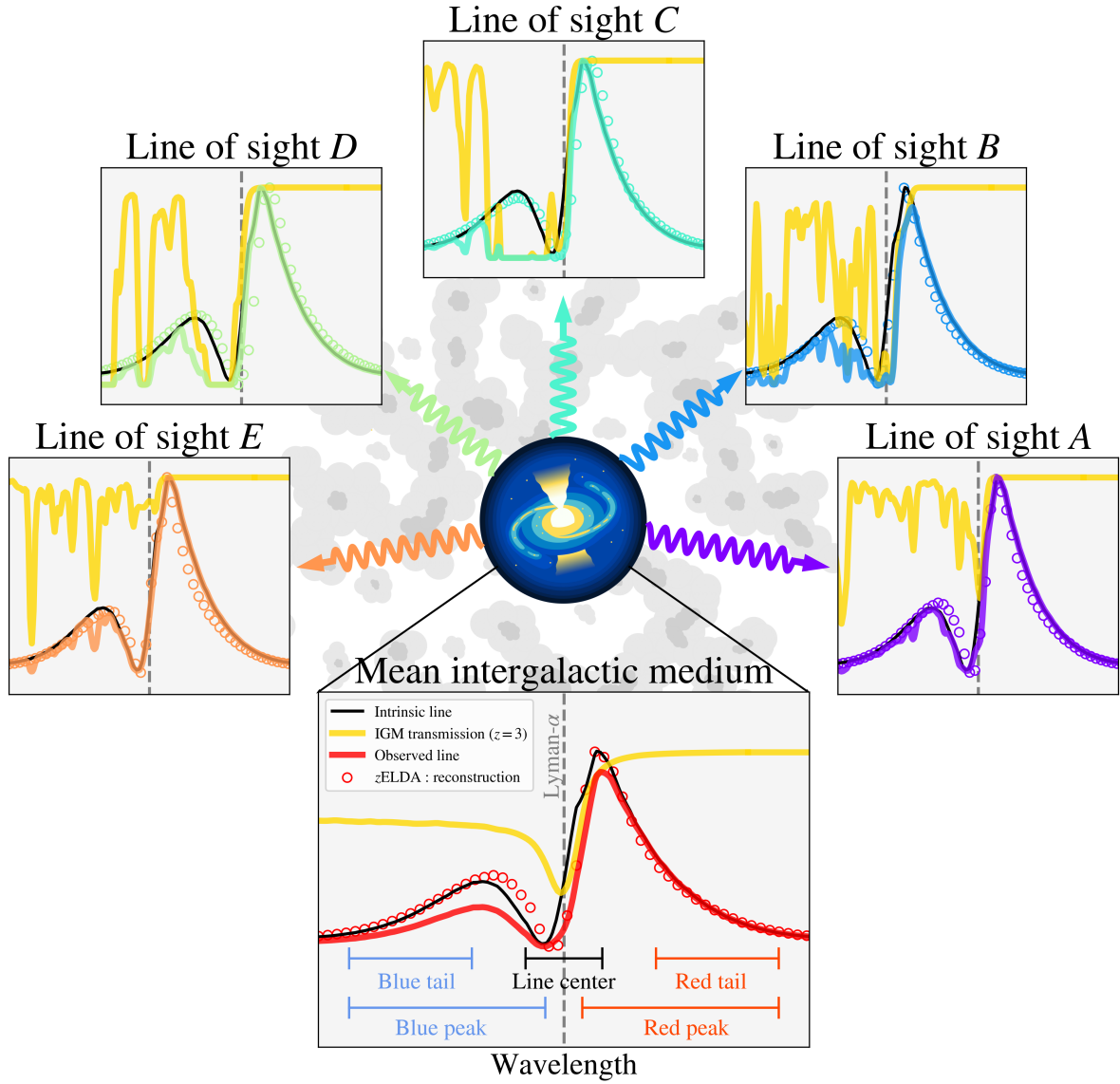


Fig. 1. Illustration of the impact of different line of sights in the same intrinsic spectrum. In the middle bottom panel we show the intrinsic spectrum escaping the source (black) convolved with the mean IGM transmission at $z = 3.0$ (yellow). The color line shows the convolution of the intrinsic spectrum and IGM transmission. The colored circles show zELDA reconstruction using the IGM- z model (discussed later). In the other top 5 panels, individual IGM transmission through different line of sights are used at $z = 3.0$.

the clumpy intergalactic medium (IGM) (Zheng et al. 2011; Laursen et al. 2011; Behrens et al. 2019; Byrohl et al. 2019; Byrohl & Gronke 2020; Gurung-López et al. 2020). A fraction of the $\text{Ly}\alpha$ photons interact with neutral hydrogen and are scattered outside the line of sight. This further modify the $\text{Ly}\alpha$ line profile shape that reaches the observer.

In fact, some theoretical works show that the measured clustering of LAEs could be potentially influenced by the radiative transfer of $\text{Ly}\alpha$. In the first place, the observability of LAEs can potentially depend on IGM the large-scale properties such as the density, velocity with respect $\text{Ly}\alpha$ sources and their gradients (Zheng et al. 2011; Behrens et al. 2019; Gurung-López et al. 2020). In second place, the determination of the redshift from the profile of the $\text{Ly}\alpha$ line profile is complex (Steidel et al. 2010; Rudie et al. 2012; Verhamme et al. 2018; Gurung-López et al. 2019a; Byrohl et al. 2019; Runnholm et al. 2021) and might in-

troduce further distortions in the measured clustering (Gurung-López et al. 2021a).

The profile of the $\text{Ly}\alpha$ line is affected at the same time by the ISM and IGM. This makes challenging the study of each of these mediums independently of the rest of the observed $\text{Ly}\alpha$ line profile. There are works that analyze possible correlation between galaxy properties and the features of the $\text{Ly}\alpha$ line profile (Hayes et al. 2023, e.g.) at $z < 0.5$, where the IGM is mostly transparent to $\text{Ly}\alpha$. However, in order to conduct the same study at high redshift, it would be ideal to have access to the $\text{Ly}\alpha$ line profile emerging from the ISM, without the influence of the IGM. At the same time, disentangling between the contributions of the ISM and the IGM would provide the IGM selection function on LAEs. This could clarify whether $\text{Ly}\alpha$ visibility depends on the large-scale properties of the IGM. Therefore, splitting the $\text{Ly}\alpha$ line profile by the contributions of ISM, IGM will be key in future works based on $\text{Ly}\alpha$ emission.

The Ly α radiative transfer process is nontrivial and only few analytical solutions exist in relatively simple gas geometries (e.g., Neufeld 1990; Dijkstra et al. 2006). Due to the complexity of solving the radiative transfer equations analytically, typically Monte Carlo radiative transfer codes are being employed. Ly α Monte-Carlo radiative transfer, although typically computationally expensive, allows for a large flexibility in gas properties and specially in gas geometry, allowing from the relatively simple ‘shell model’ (ISM/CGM), a moving spherical shell which surrounds a Ly α emitting source (Ahn 2003), to the intricate ISM, CGM and IGM gas distributions in cosmological simulations (Byrohl et al. 2019).

The ‘shell-model’ has been very successful in reproducing the shape of the observed Ly α line profiles across the Universe (e.g., Verhamme et al. 2007; Schaerer et al. 2011; Gronke 2017; Gurung-López et al. 2022). The radiative transfer process in the clumpy and intricate ISM and inner CGM is intrinsically different from that taking place in the smoother and colder IGM. In principle, the low redshift ($z < 0.5$) observed Ly α line profiles should be dominated by the radiative transfer in the ISM. However, at high redshift, the Ly α line profile should be affected by the radiative transfer in the ISM, CGM and IGM.

The use of mean IGM transmission curves might work on stacked line profiles, but for individual sources it is a very limited technique given the huge diversity of the IGM at the same redshift and even for the same source Byrohl & Gronke (2020). This is illustrated in Fig. 1 where the same Ly α line profile emerging from the ISM (black) is convolved with the mean IGM transmission at $z = 3$ (bottom panel) and five line of sights (*A* to *E*) and their individual IGM transmission curves (yellow). The line profile emerging from the IGM is shown as solid colored lines, while the reconstruction of the code presented in this work is displayed as colored empty circles. In addition, a sketch of the parts of the Ly α line profile can be found in the bottom panel. While applying the mean IGM transmission modulates the Ly α line profile smoothly, the IGM features in the individual line of sight (LoS) are sharper. This is especially noticeable in LoS *B* and *D*. In addition, the IGM topography is quite diverse, even for the same source. While there will be LoS with almost no neutral hydrogen (LoS *A*), other will be very optically thick (LoS *C*). Thus, the IGM emerging Ly α line profile depends on the individual LoS and could exhibit a huge variety even if the ISM emerging line profile is assumed to be the same. This also shows the limitation of reconstructing IGM attenuated Ly α line profiles using the mean IGM transmission at the source redshift.

In this work, we present the second version of zELDA (based on Gurung-López et al. 2022), an open source Python package based on LyART (Orsi et al. 2012) and FLAREON (Gurung-López et al. 2019a). zELDA has two main scientific motivations i) modeling Ly α line profiles and escape fraction using the shell model for cosmological simulations and (as in Orsi et al. 2014; Gurung-López et al. 2019b, 2021a,b), ii) fitting observed Ly α line profiles to the shell model. In the first version of zELDA we focused on modeling the Ly α spectrum affected only by the ISM. zELDA was able to nicely fit observed Ly α line profiles at $z < 0.5$. In the version presented here, we focus on fitting Ly α line profiles affected by ISM and IGM. For this, we make use of machine learning algorithms in which the input is basically the observed spectrum, convoluted with IGM and ISM. In Fig. 1 we show six examples of the reconstructed Ly α line profile using zELDA of the same intrinsic line profile traveling through five different lines of sights (open circles).

zELDA is publicly available and ready to use¹. zELDA contains all the scripts necessary to reproduce all the results presented in this work. Documentation and several tutorials on how to use zELDA are also available².

This work is organized as follows. In Sect. 2 we describe the data sets used to model the observed Ly α line profiles. In Sect. 3 we detail the pipeline to reconstruct the ISM emerging Ly α line profiles from the observed line profile. First, we test the accuracy of our methodology in mock Ly α spectrum in Sect. 4. Finally, we draw our conclusions in Sect. 5.

Through this work, we show Ly α line profiles and IGM transmission curves in $\Delta\lambda_0$, i.e., the rest frame difference to the Ly α wavelength. We also provide redshift accuracy in the same units. This quantity can be expressed in velocity units as $\Delta v = c\Delta\lambda_0/\lambda_{Ly\alpha} \sim (247\text{km/s}) \times \Delta\lambda/1\text{\AA}$, where c is the speed of light and $\lambda_{Ly\alpha} \approx 1215.67\text{\AA}$.

Another convention that we use through this work is the notion of ‘Ly α IGM escape fraction’. We refer to the Ly α IGM escape fraction of a source as the ratio between intrinsic and observed Ly α photons along the line of sight. We note that the Ly α photons are not, in general, destroyed by dust grains in the IGM, and hence this ratio is also referred to as the ‘transmission fraction’ in the literature. Instead, they are scattered out of the line of sight. Thus, although for the observer the IGM causes absorption features, globally, the missing photons escape the IGM in another direction.

2. Simulating Lyman alpha line profiles

In this section, we detail the data sets used to produce mock Ly α line profiles that include the ISM, CGM and IGM. In Sect. 2.1 we show the ‘shell model’ simulation that are used, based on the first zELDA version. Meanwhile, in Sect. 2.2 we detail the CGM/IGM transmission curves based on Byrohl & Gronke (2020).

2.1. Radiative transfer in the interstellar medium

As in Gurung-López et al. (2022) (hereafter ZP22), zELDA uses a set of precomputed Ly α line profiles. These lines are computed using the Monte Carlo radiative transfer code LyART (Orsi et al. 2012), which performs the entire radiative transfer computation photon by photon. This set of lines would contain the ISM radiative transfer component, while lacking the IGM influence.

The regular grid of Ly α line profiles used in this work is the same as that described in ZP22. Basically, it consists in a 5 dimensional parameter grid with 3,132,000 nodes. The 5 parameters are those of the thin shell model in LyART. These are, the outflow expansion velocity V_{exp} , the neutral hydrogen column density N_{H} , the dust optical depth τ_a , the intrinsic equivalent width EW_{in} and the line width W_{in} of the Ly α emission before entering into the thin shell. The ranges of these parameters covered by the regular grid are $V_{\text{exp}} \in [0, 1000]\text{km/s}$, $N_{\text{H}} \in [10^{17}, 10^{21.5}]\text{cm}^{-2}$, $\tau_a \in [0.0001, 0.0]$, $EW_{\text{in}} \in [0.1, 1000]\text{\AA}$ and $W_{\text{in}} \in [0.01, 6]\text{\AA}$. For further information on the grid specifications, we refer the reader to ZP22.

Ly α line profiles within the boundaries of zELDA’s grid are computed by 5D lineal interpolation between nodes, as described in ZP22. This leads to a typical accuracy of 0.04 in the Kolmogorov-Smirnov estimator (KS), which is, the maximum

¹ https://github.com/sidgl/zELDA_II

² <https://zelda-ii.readthedocs.io/index.html>

difference between cumulative distributions, in the prediction of Ly α line profiles from the thin shell model.

2.2. Radiative transfer in the intergalactic medium

In order to include radiative transfer in the intergalactic and circumgalactic medium, we make use of the transmission curves from Byrohl & Gronke (2020). These were calculated in six snapshots of the IllustrisTNG100 simulation (Naiman et al. 2018; Nelson et al. 2019; Marinacci et al. 2018; Pillepich et al. 2018; Springel et al. 2018), at redshift 0.0, 1.0, 2.0, 3.0, 4.0 and 5.0. The Ly α radiative transfer was computed using a modified version of the code ILTIS (Behrens et al. 2019; Byrohl & Gronke 2020; Byrohl et al. 2021). The radiative transfer analysis was performed for every halo with mass greater than $5 \times 10^9 M_\odot$ in 1000 different line of sight. For more information, see Byrohl & Gronke (2020).

The mean IGM transmission curves of Byrohl & Gronke (2020) are shown in the left panel of Fig. 2. These show the typical structure found in the literature, i.e., a transmission close to unity redward Ly α , a well of absorption at Ly α and a plateau at bluer wavelengths than Ly α that decreases with redshift (Laursen et al. 2011; Gurung-López et al. 2022). The shaded regions mark the 25 and 75 percentiles. As shown by Byrohl & Gronke (2020), the scatter around the mean is significant, as there is a lot of variability in the individual line of sights.

As mentioned above, the IGM transmission curves from Byrohl & Gronke (2020) are given in discrete redshift bins (0.0, 1.0, 2.0, 3.0, 4.0 and 5.0). However, for training our artificial neural networks we require a continuous redshift sampling. In order to obtain an IGM transmission curve at a given z_t we proceed as follows. First, we obtain the target mean optical depth τ_t at z_t from Faucher-Giguère et al. (2008). Next, we recalibrate the snapshot closest to z_t so that its mean optical depth matches τ_t . For this we use the wavelength range from -8\AA to -6\AA from Ly α . Finally, we draw a random IGM transmission curve.

The right panel of Fig. 2 shows the mean IGM transmission curves after the recalibration. The black horizontal lines show the mean IGM transmission by Faucher-Giguère et al. (2008). Before recalibration, we find that there is up to a 10% difference between -8 to -6\AA from Ly α . After recalibration, by construction, both mean IGM transmissions match perfectly.

Examples of the large diversity of IGM transmission curves at different redshifts are shown throughout this work. Individual IGM transmission curves are shown as solid yellow lines in Fig. 1.

2.3. Mocking observed Lyman- α line profiles

Ly α line profiles predicted by zELDA using the LyART grid of line profiles and the IGM transmission curves of Byrohl & Gronke (2020) are ideal, both in terms of spectral resolution and signal-to-noise ratio. In contrast, measurements of Ly α line profiles present limitations in the spectral resolution, spectral binning and signal to noise.

In order to produce a mock line profile of a given set of $\{V_{\text{exp}}, N_{\text{H}}, \tau_a, EW_{\text{in}}, W_{\text{in}}\}$ and through a given IGM line of sight, we follow the next procedure. First, we produce the *intrinsic* Ly α line profile escaping the galaxy from the LyART grid as described above. Second, the spectrum after traveling through the IGM is obtained by the convolution of the ideal thin shell Ly α line profile with the chosen IGM transmission curve. Third, we down-

grade the quality of the Ly α line profile to match the desired observation configuration as in ZP22.

The quality of a Ly α line profile is set by three parameters: i) the signal to noise ratio of the peak of the Ly α line, S/N_p , ii) the wavelength resolution element in the observed frame, W_g and iii) the pixel size in the observed frame, $\Delta\lambda_{\text{pix}}$. To downgrade the quality of the Ly α line profile, first we convolve the ideal spectrum with a Gaussian kernel of $\text{FWHM}=W_g$. Next, we pixelate the Ly α line profile following,

$$f_{\lambda_{\text{pix}}}^{\text{Ly}\alpha}(\lambda_{\text{pix}}) = \frac{\int_{\lambda_{\text{pix}}-\Delta\lambda_{\text{pix}}/2}^{\lambda_{\text{pix}}+\Delta\lambda_{\text{pix}}/2} f_{\lambda}^{\text{Ly}\alpha}(\lambda) d\lambda}{\Delta\lambda_{\text{pix}}}. \quad (1)$$

The intensity of the maximum of the line profile is computed and Gaussian white noise is added to the spectrum with an amplitude fixed by S/N_p . Note that in the training set $\Delta\lambda_{\text{pix}}$ and W_g are independent variables. However, in order to show the results of zELDA we fixed $\Delta\lambda_{\text{pix}} = W_g/2$ across all the plots and tables to reduce from three dimensions $\{S/N_p, W_g, \Delta\lambda_{\text{pix}}\}$ to only two $\{S/N_p, W_g\}$.

In Fig. 3 we show three spectrum quality configurations progressing from best to worst from left to right. In particular, the left column uses $S/N_p = 15.0$ and $W_g = 0.25\text{\AA}$, in the middle $S/N_p = 10.0$ and $W_g = 0.5\text{\AA}$ and in the right $S/N_p = 7.0$ and $W_g = 1.0\text{\AA}$. Ly α profiles are fixed at redshift 3.0. The intrinsic Ly α line profile emerging from the galaxy (modeled with the LyART grid) is shown in red, while a randomly chosen IGM transmission is shown in pink. The mock observed Ly α line is shown in black. The other colored lines are zELDA's reconstructions of the observed Ly α line profile that will be discussed later in Sect. 3. Basically, each row shows the same outflow configuration $\{V_{\text{exp}}, N_{\text{H}}, \tau_a, EW_{\text{in}}, W_{\text{in}}\}$, listed in Tab. C.1, in Appendix C, through the same line of sight. In the left column (cases A, D and G), the observed line profile closely follows the convolution of IGM and the intrinsic line profile. In particular, the pixel size is small in comparison with the size of the Ly α peaks. Also, most of the pixels with the peaks are above the noise. Meanwhile, the quality of the middle columns is worse. For example, the blue peak in D was clearly visible in the observations, while it is more difficult to see in E. Finally, in the right most column shows Ly α spectrum heavily affected by noise and a relatively low spectral resolution. While case F is relative well recovered given its width, the strong absorption feature present in G is mostly removed from I.

3. Reconstructing attenuated Lyman- α emission lines

In this section, we explain our methodology to reconstruct Ly α line profiles attenuated by the intergalactic medium, as well as to estimate the Ly α IGM escape fraction.

We present three models based on artificial neural networks. The idea of obtaining the redshift of a source using artificial neural networks in the Ly α line profile was initially explored in Gurung-López et al. (2021b). These models are referred to as IGM+z, IGM-z and NoIGM and have a different input and training sample. Basically, IGM+z includes the redshift of the source as input and it is trained with a realistic IGM transmission curve redshift evolution. The input of the IGM-z model does not include the redshift of the source and it is trained with redshift-randomized IGM transmission curves. Finally, the input of the NoIGM model includes the redshift of the source, but no IGM

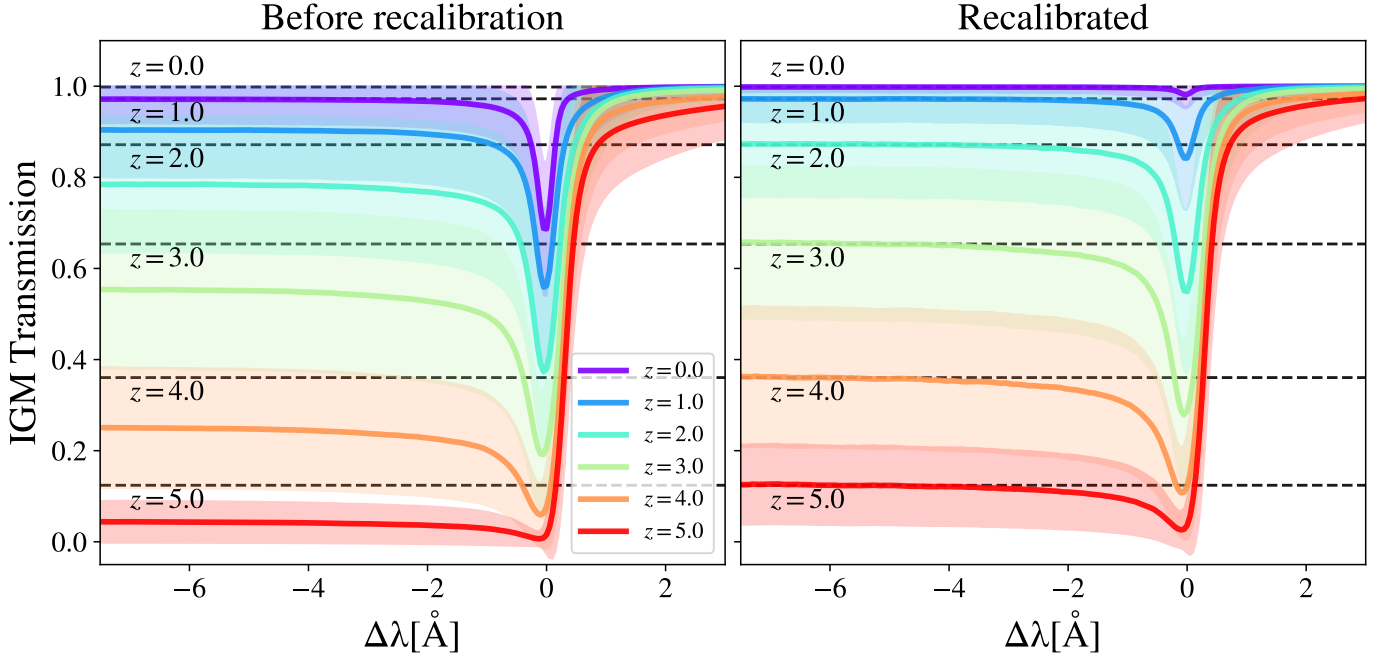


Fig. 2. Mean IGM transmission curves without recalibration (left) and after recalibration (right). Each color shows a different redshift snapshot. The horizontal black dashed show the mean IGM transmission given by (Faucher-Giguère et al. 2008) at $z = 0, 1, 2, 3, 4, 5$ from top to bottom.

transmission curve is applied to the line profiles of the training set.

This section is structured as follows. First, we detail the ANN input in Sect. 3.1, while the training sets are discussed in Sect. 3.2. Then the ANN output is described in Sect. 3.3 along with the ANNs architecture in 3.4. We present a feature importance analysis in A. Finally, the parameter estimation is shown in 3.5.

3.1. Input of artificial neural networks.

The input in the three presented models (IGM+z, IGM-z and NoIGM) follows the same philosophy as those introduced in ZP22. Basically, the input consists of the line profile and its observational quality. The main difference between the models of this work and those presented in ZP22 is how the Ly α line profile is provided to the artificial neural networks (ANN).

3.1.1. Line profile treatment

In the IGM+z, IGM-z and NoIGM models, we treat the observed line as follows:

1. The wavelength position of the global maximum of the observed line profile λ_{\max} is used as a proxy for the true Ly α wavelength λ_{true} . Thus, the proxy redshift is $z_{\max} = \lambda_{\max}/\lambda_{\text{Ly}\alpha} - 1$.
2. The observed line profile is moved to the proxy rest frame, $f_{\lambda, \max}^{\text{Ly}\alpha}$. In particular, we convert the array where $f_{\lambda}^{\text{Ly}\alpha}$ is evaluated in the observed frame, $\lambda_{\text{arr}}^{\text{Obs}}$ to the rest frame wavelength as if $\lambda_{\text{true}} = \lambda_{\max}$, i.e., $\lambda_{\text{arr}}^0 = \lambda_{\text{arr}}^{\text{Obs}}/(1 + z_{\max})$.
3. The line profile is normalized by its maximum $f_{\lambda}^{\text{Ly}\alpha}(\lambda_{\max})$.
4. The normalized line profile $f_{\lambda, \max}^{\text{Ly}\alpha}$ is rebinned into 600 bins from $\lambda_{\text{Ly}\alpha} - 12.0\text{\AA}$ to $\lambda_{\text{Ly}\alpha} + 12.0\text{\AA}$ by linear interpolation between the values of $f_{\lambda, \max}^{\text{Ly}\alpha}$ evaluated in λ_{arr}^0 .

5. The line profile is decomposed using a principal component analysis (PCA). The first 100 principal components are used, as detailed below.

Steps 1 to 4 are almost identical to those in ZP22 with only minor changes in the wavelength range used. The PCA analysis is a new addition to zELDA.

In Fig. 4 we show the total explained variance as a function of the number of principal components. We present two PCA models, one for lines without IGM (red, used for the NoIGM model) and another for lines with IGM absorption (green, used for the IGM+z and IGM-z models). We find that both PCA models exhibit the same behavior. The total explained variance grows rapidly with the first ~ 7 components up to $\sim 90\%$. After a knee, the total recovered variance grows slowly, reaching $\sim 95\%$ at 100 and $\sim 98\%$ at 400 principal components. Below 25 principal components, the total explained variance for in the lines without IGM is greater than those including the IGM for a fixed value of principal components. This seems reasonable since the IGM absorption would add complexity to the observed Ly α line profiles. From 25 principal components onward, the total variance in both models is the same.

We used the first 100 principal components in the models presented in this work. We tested that using the first 200 and 400 principal components did not increase the precision in reconstructing the intrinsic Ly α line profiles.

The right panel of Fig. 4 shows an example of the PCA decomposition of a shell model line profile that is unobscured by the IGM (grey). The different colored lines show the PCA decomposition using only the first 1, 2, 5, 10, 20, 50 and 100 components (from purple to red). The first 2 components focus on the red peak. The blue peak is progressively recovered as we increase the components from 3 to 20. The first 20 principal components give an accurate, although smoothed, version of the original line profile. Meanwhile, from the 20th up to 100th components, small features are captured, including the noise pattern.

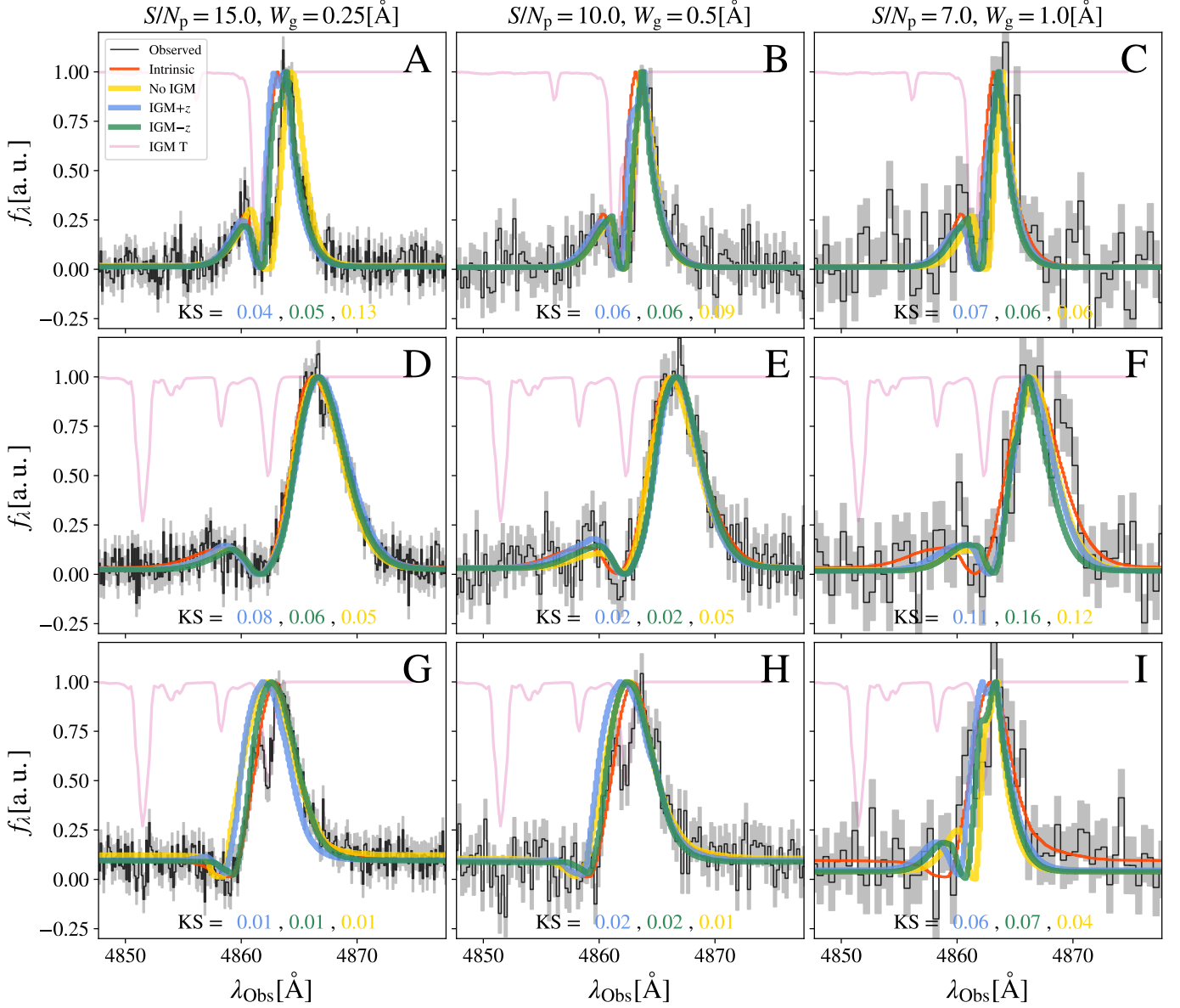


Fig. 3. Example of line profile reconstruction at different line profile qualities and using our different models. The true Ly α line before passing through the IGM is displayed in red. The IGM transmission curve is shown in pink. The true Ly α line profile is fixed in each row. The observed line profile, after IGM absorption and mocking observation conditions, is shown in black. The observation conditions are fixed in each column as $W_g = 0.25\text{\AA}$, $S/N_p = 15.0$, $W_g = 0.5\text{\AA}$, $S/N_p = 10.0$, $W_g = 1.0\text{\AA}$, $S/N_p = 7.0$, from left to right respectively. The zELDA prediction for the models IGM+z, IGM-z and NoIGM are displayed in blue, green and yellow respectively. In the bottom of each panel the KS between the true Ly α line profile before the IGM absorption and zELDA prediction is displayed in different colors matching the model used.

Although not displayed here, the IGM features are encapsulated from the 20th to 100th principal components.

3.1.2. Line profile quality and redshift

As in ZP22 we include the line profile quality as features in the input of the artificial neural networks. In particular, we include the wavelength element of resolution and the pixel size, both in the observed frame. This is the same in all three models.

Then, in ZP22 we included the redshift of the sources through the proxy z_{max} . In this work, we do the same in IGM+z and NoIGM. Meanwhile, the redshift is excluded from IGM-z. On one hand, the motivation behind IGM+z is to produce a model with the same IGM distribution as in Byrohl & Gronke (2020).

On the other hand, the goal behind IGM-z is to provide a model as unbiased as possible by the redshift-dependent quantities and that matches Faucher-Giguère et al. (2008) mean IGM transmission.

3.1.3. Total input

The input for each model is slightly different. The models IGM+z and NoIGM use 103 features:

- Input = [... 100 PCA ..., W_g , $\Delta\lambda_{\text{pix}}$, z_{max}],

However, the PCA model used for IGM+z includes the IGM absorption, while the PCA model used for NoIGM does not.

Then, the input for the IGM-z model is the same as before but excluding z_{max} , i.e., 102 features:

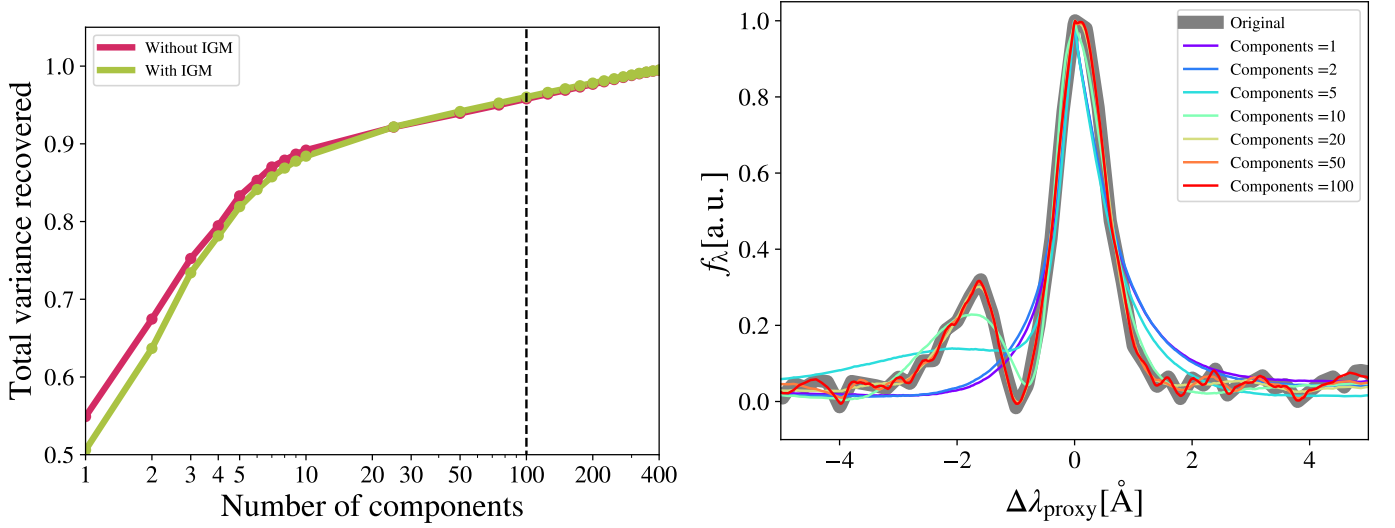


Fig. 4. Left: Total variance recovered as a function of the number of principle components. In red (green), Ly α line profiles spanning zELDA's grid without (with) IGM absorption. The dashed black line mark the number of principal components used for the input of the artificial neural networks. Right: example of the PCA decomposition in an IGM clean shell model line profile. The line profiles are shown in the proxy rest frame. The original mock line profile is shown in grey. Meanwhile, the reconstructed line profiles using the N first principal components as displayed in the legend.

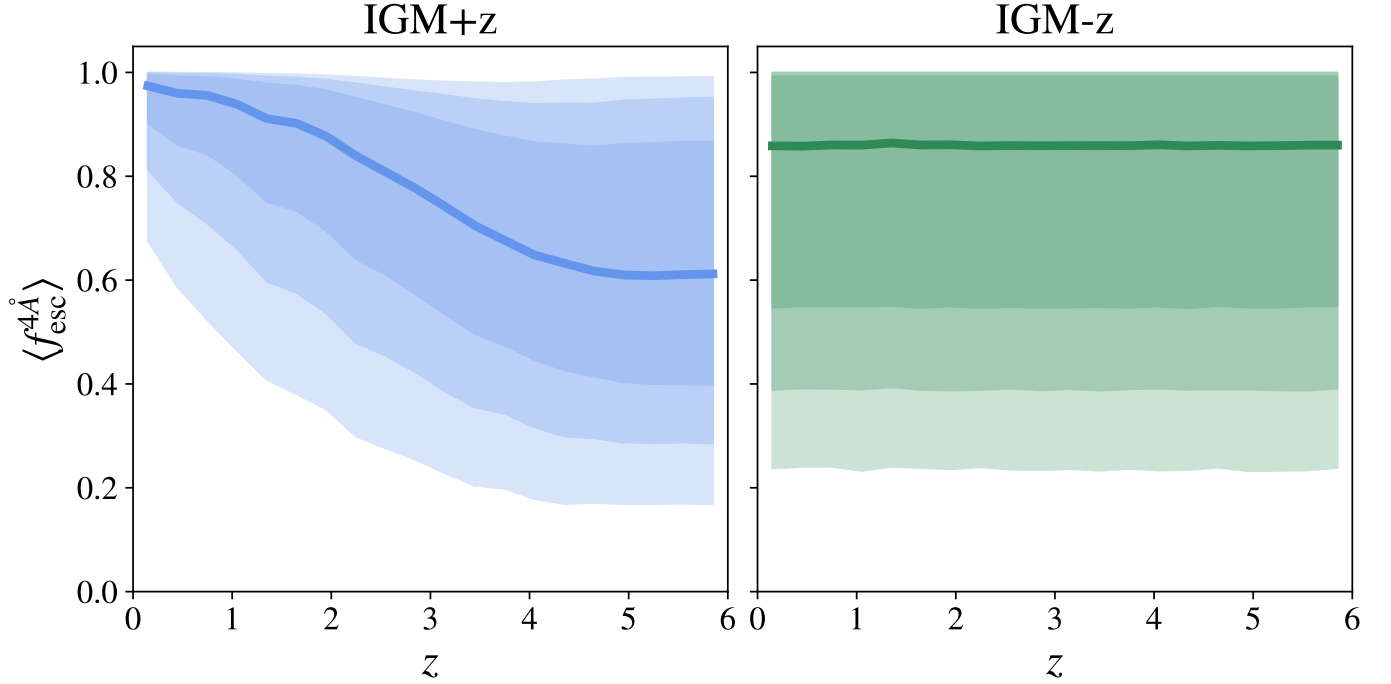


Fig. 5. $f_{\text{esc}}^{4\text{\AA}}$ used for the training in the IGM-z (left) and IGM+z (right) models. The solid thick line marks the median $f_{\text{esc}}^{4\text{\AA}}$. Meanwhile, the shaded regions show the scatter between the 16 and 84 percentiles (darkest), 5 and 95 percentiles (medium dark), 1 and 99 percentiles (clearest).

– Input = [... 100 PCA ... , W_g , $\Delta\lambda_{\text{pix}}$],

where the PCA model is the same as in IGM+z and includes the IGM absorption.

3.2. Training sets of artificial neural networks.

The training sets for IGM+z, IGM-z and NoIGM are different from each other. Nevertheless, they share the same number of Ly α line profiles (4.5×10^6) and the outflow parameters $\{V_{\text{exp}}, N_H, \tau_a,$

$EW_{\text{in}}, W_{\text{in}}\}$ are equally homogeneously randomly drawn from the space covered by the Ly α RT grid. The mock Ly α line profiles cover uniformly from $W_{\text{in}}=0.01\text{\AA}$ to 4.0\AA , $\Delta\lambda_{\text{pix}}=0.01\text{\AA}$ to 2.0\AA and from $S/N_p=5.0$ to $S/N_p=15.0$. We tested that for this training set size, our artificial neural networks have converged. In addition, for the three models, redshifts from 0 to 6 were homogeneously sampled. Notice that the IGM transmission curves from Byrohl & Gronke (2020) are computed up to the snapshot at $z=5$. Therefore, the predictions given by IGM+z and IGM-z

at $z > 5$ should be taken with caution. The particularities of the training sets, therefore, depend on how the IGM is treated:

- **IGM+z:** This training set includes line profiles with the IGM absorption. In this model, we use the uncalibrated IGM transmission curves. In particular, the IGM transmission curve to each Ly α line profile uses the actual redshift of the source. Therefore, there is an evolution in the IGM where Ly α line profiles at higher redshift are more attenuated.
- **IGM-z:** This training set also includes line profiles with the IGM absorption. However, in contrast to IGM+z, we use the recalibrated transmission curves, which are drawn randomly irrespective of the source redshift. Thus, the IGM absorption distribution is constant with redshift. There will be Ly α basically unabsorbed (typical of $z = 0$) and greatly absorbed (typical of high z) at all redshifts.
- **NoIGM:** This training set does not use IGM transmission curves.

In Fig. 5 we compare the distribution of $f_{\text{esc}}^{4\text{\AA}}$ (IGM Ly α escape fraction $\pm 2\text{\AA}$ around Ly α) as a function of redshift in the training sets for the IGM+z (left) and IGM-z (right). The model IGM+z exhibits an evolution in the median $f_{\text{esc}}^{4\text{\AA}}$ as a function of the redshift, given by the evolution of the opacity of IGM. At $z < 1$ the median $f_{\text{esc}}^{4\text{\AA}}$ is close to 1.0 while at $z > 4.0$ it stalls at 0.6. In particular, there is no evolution from $z = 5.0$ to $z = 6.0$ as the last snapshot with IGM transmission curves is at $z = 5.0$. Meanwhile, at $z < 0.5$ the training set for IGM+z shows less scatter than at high redshift, exhibiting more than 98% of the sample with $f_{\text{esc}}^{4\text{\AA}} > 0.6$. Then, at higher redshift the scatter increases and at $z = 4$ as 98% of the sample is between 1.0 and 0.2. Then, focusing on IGM-z, as the redshift of the IGM transmission curve is randomized, there is no evolution in the distribution of $f_{\text{esc}}^{4\text{\AA}}$ as a redshift function. The IGM-z model is conceived as a ‘redshift unbiased’ model.

The IGM+z and IGM-z models have the same global motivation: reconstructing an IGM attenuated Ly α line profile and obtaining the IGM escape fraction. IGM+z and IGM-z are complementary to each other. In machine learning, the input features and the training set are very important for the output of the neural networks. If a training set exhibits some particular biases, the output can potentially show the same biases. In principle, IGM+z uses in the input the proxy redshift of the source and the evolution of the IGM transmission curves with redshift of the IllustrisTNG100 simulation Byrohl & Gronke (2020). Furthermore, in Appendix A we performed a feature importance analysis on IGM+z, IGM-z and NoIGM, finding that the input proxy redshift had a strong influence in the determination of the outflow parameters and especially in $f_{\text{esc}}^{4\text{\AA}}$. Thus, the output of IGM+z can potentially be biased towards the IGM redshift evolution in Byrohl & Gronke (2020). For these reasons, we developed IGM-z, which does not include the proxy redshift in the input and has no IGM redshift evolution in the training set. Thus, IGM-z should be a redshift unbiased model. In the following sections, we compare the results obtained by IGM+z and IGM-z, finding that both perform really similarly with only small differences at $z < 1$. Finally, we remark that if a redshift-dependent evolution (e.g. on V_{exp} or $f_{\text{esc}}^{4\text{\AA}}$) is found by both, IGM+z and IGM-z, this would give robustness to the result.

3.3. Output of artificial neural networks

The three models IGM+z, IGM-z and NoIGM have a similar output, almost like the ANN in ZP22. As in ZP22, there are five out-

put variables associated to the outflow configuration $\{V_{\text{exp}}, N_{\text{H}}, \tau_a, EW_{\text{in}}, W_{\text{in}}\}$. In order to estimate the redshift of the source, another output is the difference between the wavelength set as Ly α and the true Ly α wavelength in the proxy rest frame, $\Delta\lambda_{\text{True}}$. The true Ly α wavelength in the observed frame, $\lambda_{\text{True}}^{\text{Obs}}$, can be recovered as

$$\Delta\lambda_{\text{True}} = \lambda_{\text{True}}^0 - \lambda_{\text{Ly}\alpha} = \lambda_{\text{Ly}\alpha} \left(\frac{\lambda_{\text{True}}^{\text{Obs}}}{\lambda_{\text{max}}} - 1 \right), \quad (2)$$

Then, the redshift of the source is $z = \lambda_{\text{True}}^{\text{Obs}} / \lambda_{\text{Ly}\alpha} - 1$. For further details see Gurung-López et al. (2022).

In the case of IGM+z, IGM-z we included additional variables. In each of the Ly α line profiles used for the training set, we measure the fraction of photons that escape the IGM in wavelength intervals centered around Ly α . We refer to these variables as $f_{\text{esc}}^{x\text{\AA}}$ where x is the width of the wavelength window in rest frame used. For example, $f_{\text{esc}}^{4\text{\AA}}$ is the Ly α IGM escape fraction in $\lambda_{\text{Ly}\alpha} \pm 2\text{\AA}$ in rest frame. zELDA’s IGM+z, IGM-z models include wavelength windows from 1\AA to 10\AA . We find that for a wavelength window of 4\AA the Ly α IGM escape fraction converge. Increasing the window size does not increase $f_{\text{esc}}^{x\text{\AA}}$. Also, up to a wavelength window of 4\AA the escape fraction increases with window size. This is reasonable since the mean IGM transmission curves show a drop close to the center of the Ly α line, then stabilize to the cosmic mean IGM transmission.

3.4. Architecture of artificial neural networks.

For each output property, we trained an independent ANN. We tested different configurations. We found that for $\{V_{\text{exp}}, N_{\text{H}}, \tau_a, EW_{\text{in}}, W_{\text{in}}\}$ and $f_{\text{esc}}^{x\text{\AA}}$ the best configuration was a three-layer ANN with sizes (103, 53, 25). Meanwhile, for $\Delta\lambda_{\text{True}}$ we found that a nine layer ANN had the best accuracy with sizes (103,90,80,70,60,50,40,30,20).

We have performed a feature importance analysis in Appendix A. Overall, we find that the region $\pm 4\text{\AA}$ around the Ly α alpha wavelength contains the most important information for most predicted shell parameters.

3.5. Redshift, outflow and IGM escape fraction estimation

The shell properties $V_{\text{exp}}, N_{\text{H}}, \tau_a, EW_{\text{in}}, W_{\text{in}}$ and the IGM escape fractions $f_{\text{esc}}^{x\text{\AA}}$ and $\Delta\lambda_{\text{True}}$ are obtained as the median of the distribution of outputs resulting from the ANN using as input 1000 perturbations of the original observed Ly α line profile by its noise pattern (as in Gurung-López et al. 2022). The percentiles 16 and 84 are used as the 1σ uncertainty of these properties. In ZP22 we demonstrated that this methodology achieves better accuracy in contrast to directly using the ANN output of a single realization. Additionally, making multiple iterations provides the uncertainty for the measurement. This is further discussed in Appendix B.

4. Results on mock Lyman- α line profiles

In this section, we show the results of the three ANN models presented in this work on mock observed Ly α line profiles. First, we characterize the accuracy in reconstructing the line profiles in Sect. 4.1. Then we show the performance of zELDA in recovering the evolution of the IGM escape fraction through time in

Sect. 4.2. Finally, analyze zELDA's capability to reconstruct the intrinsic stack spectrum emerging from galaxies and before the IGM radiative transfer in Sect. 4.3.

4.1. Accuracy of the ANN models

Here we characterize the accuracy of IGM+z, IGM-z and NoIGM for recovering the redshift, outflow parameters and Ly α IGM escape fraction. First, we show some individual examples. Further details on the accuracy of each parameter are given in Appendix C. Moreover, we show the precision in the recovered line profile shape in Appendix D.

In Fig. 6 we display 20 individual mock line profiles that were successfully reconstructed by zELDA's IGM+z, IGM-z models. In each panel, the intrinsic Ly α line profile leaving the galaxy is shown in red, while the IGM transmission curve is shown in pink. The mock observed Ly α line profiles used to build the input for the ANN models are shown in black. The quality of the mock line profiles is $S/N_p = 15.0$, W_g is $0.1(1+z)$ so that the resolution element is constant in rest frame, and $\Delta\lambda_{\text{pix}} = W_g/2$. zELDA's prediction using IGM+z, IGM-z and NoIGM are displayed in blue, green and yellow, respectively. The true $f_{\text{esc}}^{4\text{\AA}}$ is shown in black, while the predictions of IGM+z, IGM-z are given in top blue and bottom green, respectively, with their 1σ uncertainty. Kolmogorov-Smirnov is shown for IGM+z, IGM-z and NoIGM, from left to right, between the predicted line and the intrinsic (red).

Ly α line profiles in Fig. 6 are typically reconstructed by IGM+z, IGM-z with $KS < 0.1$. Both, the red peaks and the blue peak are properly recovered at the same time. For example, in cases *E* and *I* the observed Ly α line profiles still show some hints of the existence of a blue peak previously to the IGM. IGM+z, IGM-z and reconstruct quite well the intrinsic blue peak. However, despite the general good reconstruction of the blue peaks, sometimes IGM+z or IGM-z underpredict the blue peaks (case *S*). This tends to happen when the IGM absorption is so strong that most of the blue peak information is erased from the observed spectrum. However, it is remarkable that even in some scenarios of heavy IGM attenuation, both the blue and red peaks are properly reconstructed (cases *J*, *N*, *O*, *P* and *R*). Moreover, in some extreme cases where half or more of the line is obscured (cases *P*, *Q*, *S* and *T*), the Ly α line profiles are reconstructed with typical $KS < 0.8$.

Meanwhile, NoIGM works relatively well at low redshift (cases *A*, *B*, *C*). However, NoIGM fails to recover the intrinsic Ly α line profiles of the heavily attenuated observed Ly α line profiles. In fact, the red peaks are relatively well fitted, while the blue peaks are poorly reconstructed (cases *L*, *M*, *P*, *R*, *S*). There are some cases in which NoIGM fails to reconstruct the red peak of the line (cases *Q*, *T*) as well.

The examples in Fig. 6 demonstrate two key aspects of the Ly α line profile reconstruction. First, Fig. 6 shows that in some cases, the IGM attenuation can reshape a thin shell Ly α line profile into another Ly α line profile similar to another thin shell configuration. This is made evident by comparing the NoIGM output to the observed lines in cases *K*, *L*, *M*, *N*, *R* and *S*. Second, notice that especially in examples *K*, *L* and *N* the red peak of the observed line profile is well fitted by the three models, including NoIGM. NoIGM gives a different prediction for the blue peak than IGM+z and IGM-z. This shows that the observed red peak degenerates with the intrinsic blue peak. These two facts result in a, perhaps inevitable, confusion in the reconstructed shell param-

eters, redshift and Ly α IGM escape fraction for some observed Ly α line profiles.

Fig. 7 shows some cases where the line profile reconstruction by IGM+z, IGM-z could be considered deficient or improvable ($KS > 0.1$). The color code follows Fig. 6. In general, we find that IGM+z, IGM-z success or fail in the same line profiles. Only in a few cases IGM+z or IGM-z accurately recover the intrinsic line (e.g. $KS = 0.04$) and the other IGM model gives an inaccurate reconstruction (e.g. $KS = 0.2$). IGM+z, IGM-z tend to give worse predictions when the observed line after IGM absorption resembles that of a wrong outflow model (here, especially cases *A* and *D*). Another source of inaccuracy is the complete destruction of the blue side information, leading to an over/underprediction of the Ly α blue peak (cases *F* and *G*). In general, we also find that the NoIGM model does not recover the correct intrinsic line profile when IGM+z and IGM-z do.

We study the ratio between successful and unsuccessful reconstructions. For simplicity, we use $KS = 0.1$ as a threshold to distinguish between successful and unsuccessful reconstructions. We find that the fraction of sources with $KS < 0.1$ (properly recovered) depends on the quality of the Ly α line profile. The better the spectral quality, the higher the fraction of sources with $KS < 0.1$. Taking into account IGM+z and IGM-z, the fraction for sources with $KS < 0.1$ is greater than 90% for many of the quality configurations explored. We find that a good fraction of the line profiles are properly recovered even at relatively bad spectral quality. In particular, we find that for $S/N_p > 7.5$ and $f_{\text{esc}}^{4\text{\AA}} > 0.5$ the $Q(KS = 0.1) > 70\%$ typically, even at $W_g = 4.0\text{\AA}$. More details can be found at Appendix D.

4.2. Reconstructing the IGM escape fraction evolution

In this section, we explore zELDA's capability to measure the $f_{\text{esc}}^{4\text{\AA}}$ evolution through cosmic time. For this purpose, we develop mock samples of Ly α line profiles with different IGM escape fraction redshift dependences and analyze zELDA's performance on these mocks.

4.2.1. Mean Ly α IGM escape fraction redshift dependence reconstruction.

In this section, we study the capabilities of zELDA to reconstruct the redshift evolution of the mean $f_{\text{esc}}^{4\text{\AA}}$. For this goal, we develop Ly α line profile mock samples with different mean $f_{\text{esc}}^{4\text{\AA}}$ evolution. Later, we study the accuracy of IGM+z and IGM-z in these mocks.

We parameterize the mean $f_{\text{esc}}^{4\text{\AA}}$ redshift dependence as a Fermi-Dirac distribution, i.e.,

$$\langle f_{\text{esc}}^{4\text{\AA}} \rangle = \frac{1}{e^{b(z-a)} + 1}, \quad (3)$$

where a and b are two free parameters. The Fermi-Dirac distribution was chosen to reproduce the expected average evolution from an opaque ($f=0.0$) to transparent IGM ($f=1.0$) with an asymptotic behavior on both ends.

For a given combination of parameters a and b we generate a set of 500 Ly α line profiles homogeneously distributed from $z = 0$ to 6. Each Ly α line profile at redshift z_1 is assigned an IGM transmission curve at a random redshift z_2 . Next, the outflow line profile (intrinsic) is convolved with the chosen IGM transmission curve and $f_{\text{esc}}^{4\text{\AA}}$ is measured. If the computed $f_{\text{esc}}^{4\text{\AA}}$ is

Successful reconstruction

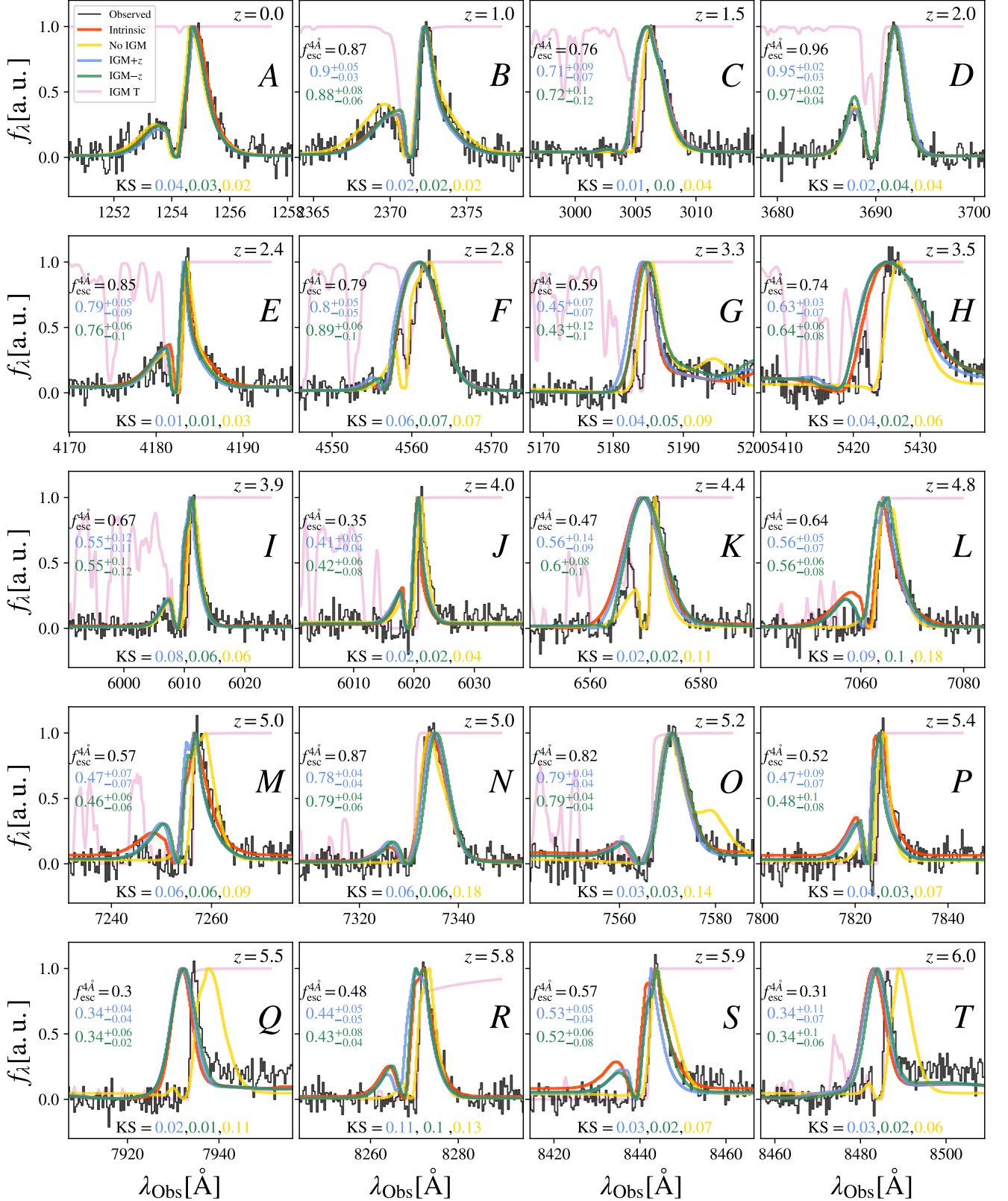


Fig. 6. Examples of line profile successful reconstruction at different redshift. The redshift of the mock line profile is in the top right corner of each subpanel. The Ly α line after the ISM and before traveling through the IGM is shown in red. The IGM transmission curve is shown in pink. The observed line profile, after IGM absorption and mocking observation conditions, is shown in black. $S/N_p = 15.0$ is fixed for all the line profiles. Meanwhile, W_g is $0.1(1+z)$ so that the resolution element is constant in rest frame. zELDA's prediction for the models IGM+z, IGM-z and NoIGM are displayed in blue, green and yellow, respectively. In each panel the true $f_{\text{esc}}^{4\text{\AA}}$ is displayed in black while zELDA's predictions are shown in color text matching the model used with their uncertainties below it. In the bottom of each panel the KS between the true Ly α line profile before the IGM absorption and zELDA prediction is displayed in different colors matching the model used.

Unsuccessful reconstruction

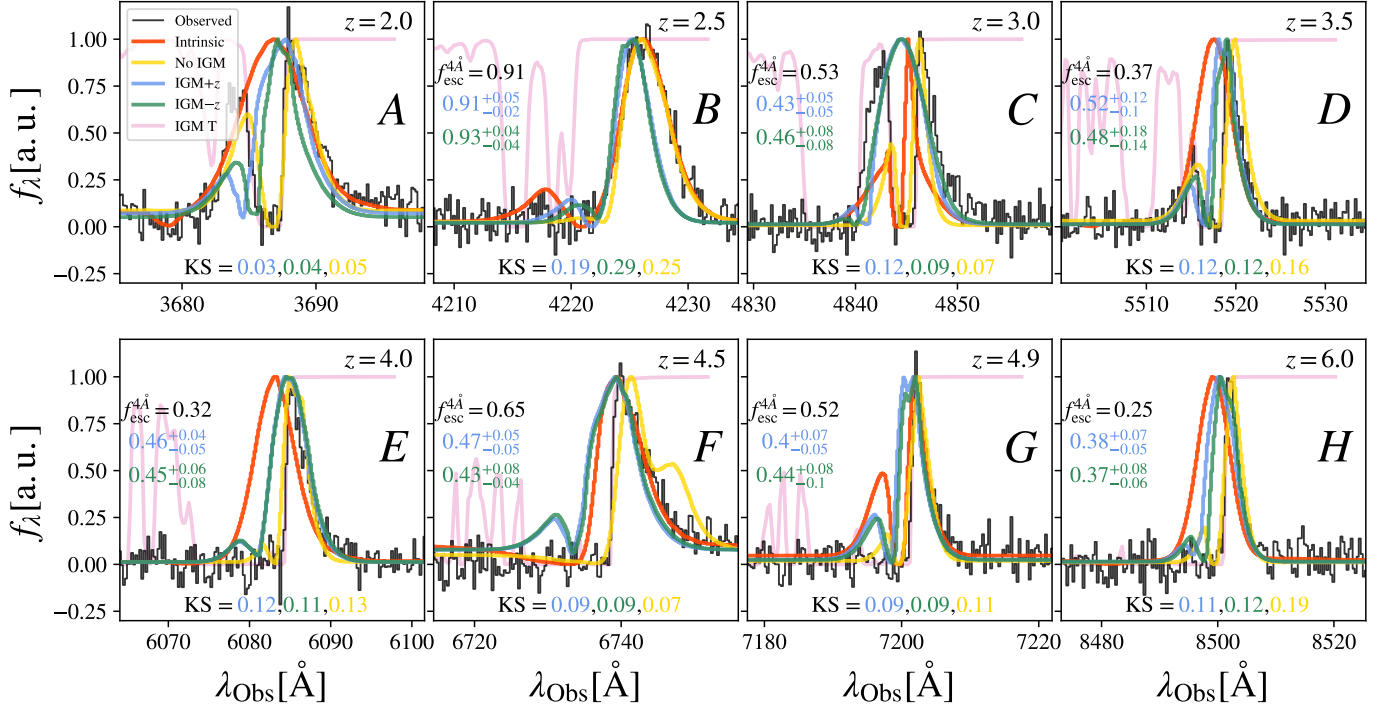


Fig. 7. Same as Fig. 6 but for unsuccessful reconstructions.

within 10% of the $\langle f_{\text{esc}}^{4\text{\AA}} \rangle(z_1)$, then this Ly α line profile is accepted as valid. However, if this condition is not met, a new IGM transmission curve at another random redshift z_3 is assigned until the condition is fulfilled. By construction, all Ly α line profiles will exhibit $f_{\text{esc}}^{4\text{\AA}}$ values close to the Fermi-Dirac with parameters a and b .

We have produced Ly α line profile mocks for four a and b combinations that populate the $\langle f_{\text{esc}}^{4\text{\AA}} \rangle$ - z space. In Figs. 8 and 9 we show four $\{a, b\}$ combinations, which are Mock1 {7.0, 0.7} (green), Mock2 {6.0, 0.6} (red), Mock3 {5.0, 0.5} (blue) and Mock4 {4.0, 0.4} (grey). For each a and b combination, we produce mocks with six spectral quality configurations. For $S/N_p = 10.0$ (left column) and $S/N_p = 15.0$ (right column) three values of W_g are run, 0.1 \AA , 1.0 \AA and 2.0 \AA from top to bottom. The colored solid lines show the parametric $\langle f_{\text{esc}}^{4\text{\AA}} \rangle$ and the colored squares the actual $\langle f_{\text{esc}}^{4\text{\AA}} \rangle$ in that redshift bin.

In Fig. 8 we show the IGM+z prediction for the mock samples. The colored crosses show the $f_{\text{esc}}^{4\text{\AA}}$ predictions line per line. The colored circles mark IGM+z's estimations of $\langle f_{\text{esc}}^{4\text{\AA}} \rangle$ in the same redshift bins as for the true values. Meanwhile, the results for IGM-z are shown in Fig. 9. In general, we find that both IGM+z and IGM-z recover the $\langle f_{\text{esc}}^{4\text{\AA}} \rangle$ evolution with redshift. For both models, the precision of the reconstructed $\langle f_{\text{esc}}^{4\text{\AA}} \rangle$ evolution changes with the spectral quality. For line with higher resolution and S/N_p the recovered $\langle f_{\text{esc}}^{4\text{\AA}} \rangle$ follows well the true $\langle f_{\text{esc}}^{4\text{\AA}} \rangle$ evolution. However, when the spectral quality decreases, some biases appear in the $\langle f_{\text{esc}}^{4\text{\AA}} \rangle$ estimate. We also find that IGM+z and IGM-z show a limitation for low $f_{\text{esc}}^{4\text{\AA}}$ values (~ 0.4). For example, at $S/N_p = 15.0$, $W_g = 0.1\text{\AA}$, $\langle f_{\text{esc}}^{4\text{\AA}} \rangle$ stales at ~ 0.45 at redshift ~ 5 in Mock4 while it should fall down to 0.3. Also, for the worst

spectral quality configuration ($W_g = 2.0\text{\AA}$) we find that, while the general $\langle f_{\text{esc}}^{4\text{\AA}} \rangle$ redshift evolution is recovered, $\langle f_{\text{esc}}^{4\text{\AA}} \rangle$ is slightly biased for Mock1 and Mock4. In particular, the results in Mock1 are up to a $\sim 10\%$ under predicted, while those for Mock4 are up to a $\sim 10\%$ over predicted. Meanwhile, the results for Mock2 and Mock3 for $W_g = 2.0\text{\AA}$ is quite unbiased and most individual measurements are 1σ compatible with the true values.

We find that while the S/N_p of the line has an impact on the accuracy of the recovered $\langle f_{\text{esc}}^{4\text{\AA}} \rangle$, W_g has a greater influence. This is also found when determining $f_{\text{esc}}^{4\text{\AA}}$ in individual line profiles. As shown in Fig. C.2, focusing in the $f_{\text{esc}}^{4\text{\AA}} \in [0.95, 1.0]$ regime, for $W_g = 0.1\text{\AA}$, changing S/N_p from 15.0 to 5.0 produces a drop in $f_{\text{esc}}^{4\text{\AA}}$ accuracy from 0.03 to 0.04. However, for $S/N_p = 10.0$, the $f_{\text{esc}}^{4\text{\AA}}$ accuracy at $W_g = 0.25\text{\AA}$ is 0.03, while at $W_g = 2.0\text{\AA}$ is 0.1. This becomes even more apparent in the $f_{\text{esc}}^{4\text{\AA}} \in [0.65, 0.8]$, where there is no clear $f_{\text{esc}}^{4\text{\AA}}$ accuracy dependence on S/N_p , while it gets worse for larger W_g values.

In general, Fig. 8 shows that the IGM+z model provide an accurate $\langle f_{\text{esc}}^{4\text{\AA}} \rangle$ estimation for the explored mocks at $W_g = 0.1\text{\AA}$, as most of the measurements are 1σ compatible with the true values. Moreover, IGM+z provides a relatively unbiased and accurate prediction between redshifts 2 and 5 for the four mocks presented and for all spectral quality configurations. However, we find that the IGM+z model is biased at $z < 1$ at every explored spectral quality (e.g. Mock3 and Mock4). IGM+z tends to over predict $\langle f_{\text{esc}}^{4\text{\AA}} \rangle$ and gives values close to unity at this redshift range. This bias becomes stronger as the spectral quality decreases. For example, at $z = 1$ and $W_g = 0.1\text{\AA}$, $\langle f_{\text{esc}}^{4\text{\AA}} \rangle$ is over predicted a $\sim 10\%$. Nevertheless, the general trend ($\langle f_{\text{esc}}^{4\text{\AA}} \rangle$ de-

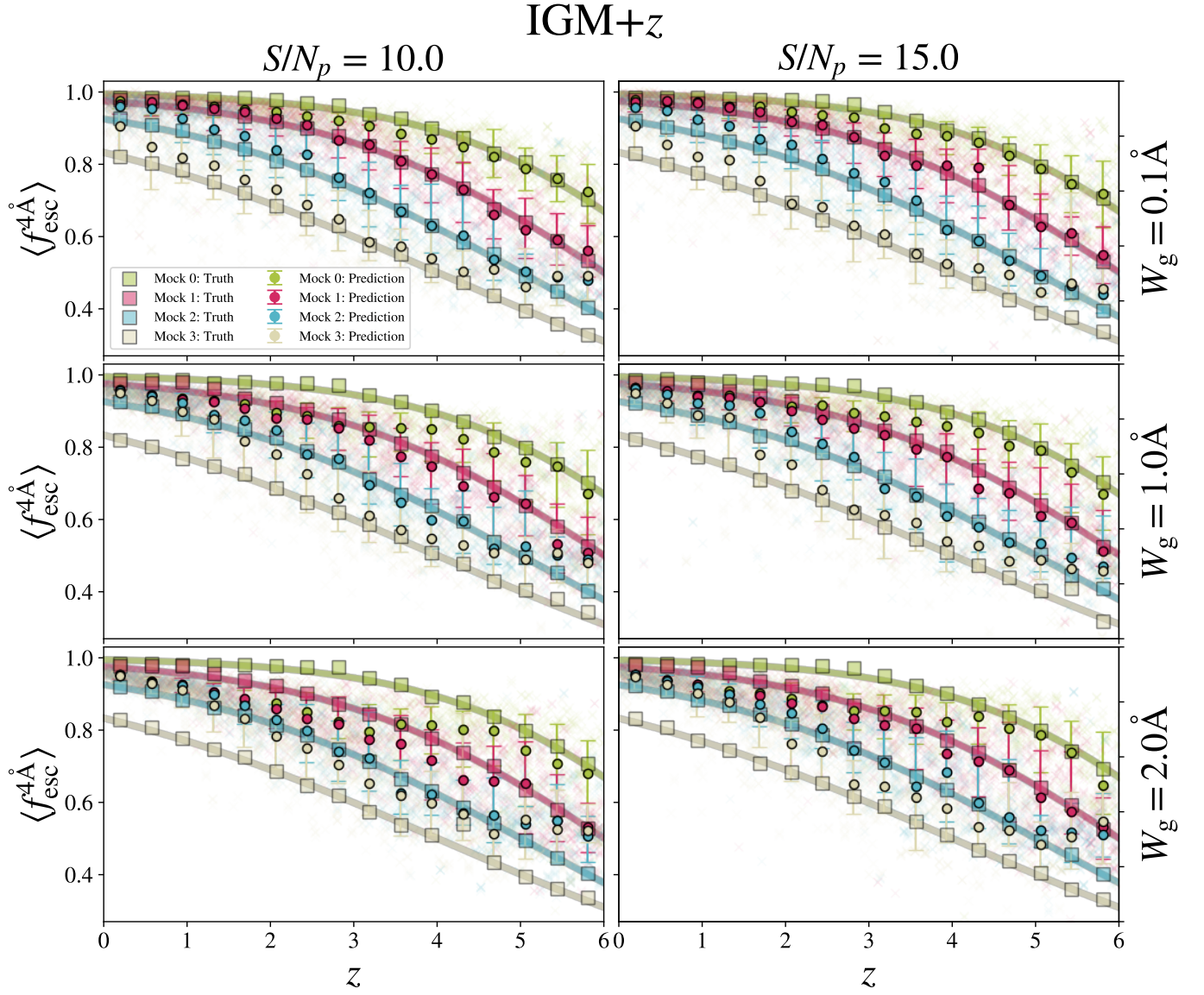


Fig. 8. zELDA's prediction on the mean $f_{\text{esc}}^{4\text{\AA}}$ for different mock Ly α line profiles using the IGM+z model. Each panel shows a different observation quality. The left and right column display $S/N_p = 10.0$ and $S/N_p = 15.0$, respectively. Each row has a constant W_g . In particular, $W_g = 0.1\text{\AA}$, 1.0\AA and 4.0\AA , from top to bottom. Four mean $f_{\text{esc}}^{4\text{\AA}}$ z evolution scenarios are considered, which are shown in solid lines (green, red, blue and grey). The true mean $f_{\text{esc}}^{4\text{\AA}}$ in the mocks is shown in colored squares. zELDA's predictions for individual Ly α line profiles are marked as crosses. The mean $f_{\text{esc}}^{4\text{\AA}}$ from zELDA's prediction is shown in circles with its uncertainty.

creases with z) is recovered in all spectral quality configurations and redshift bins.

Focusing in IGM-z (Fig. 9), $\langle f_{\text{esc}}^{4\text{\AA}} \rangle$ is nicely recovered for $W_g = 0.1\text{\AA}$ and $S/N_p = 10.0$ and $S/N_p = 15.0$ for the explored evolution cases. Also, we find that IGM-z is less biased toward $\langle f_{\text{esc}}^{4\text{\AA}} \rangle = 1.0$ than IGM+z at low redshift. For example at $W_g = 0.1\text{\AA}$, the $\langle f_{\text{esc}}^{4\text{\AA}} \rangle$ evolution in Mock4 is recovered almost perfectly with no apparent bias at $z < 1$. For $W_g = 1.0\text{\AA}$, $\langle f_{\text{esc}}^{4\text{\AA}} \rangle$ is a 10% overestimated for Mock4 at $z < 1$. Moreover, unlike for IGM+z, at $z < 1$ the rank order in $\langle f_{\text{esc}}^{4\text{\AA}} \rangle$ is recovered properly. Individual measurements of Mock1 are greater than those of Mock2, which are greater than those of Mock3, which are above those of Mock4. Furthermore, at $z > 1$ we find the same trends as in IGM+z.

Table 1. Outflow parameters in the redshift nodes used for the Ly α line profile stacked mocks.

z	V_{exp} [km s $^{-1}$]	$\log N_{\text{H}}$ [cm $^{-2}$]	EW_{in} [\AA]	W_{in} [\AA]	τ_a
0.0	200.0	19.3	18.0	2.0	0.01
1.0	125.0	19.9	12.0	0.7	1.0
2.0	190.0	20.7	50.0	1.6	0.02
3.0	40.0	19.1	1.0	0.25	0.0004
4.0	70.0	18.2	12.	1.6	0.5
5.0	70.0	20.3	9.0	1.6	0.0001
6.0	170.0	19.3	300	1.75	0.0004

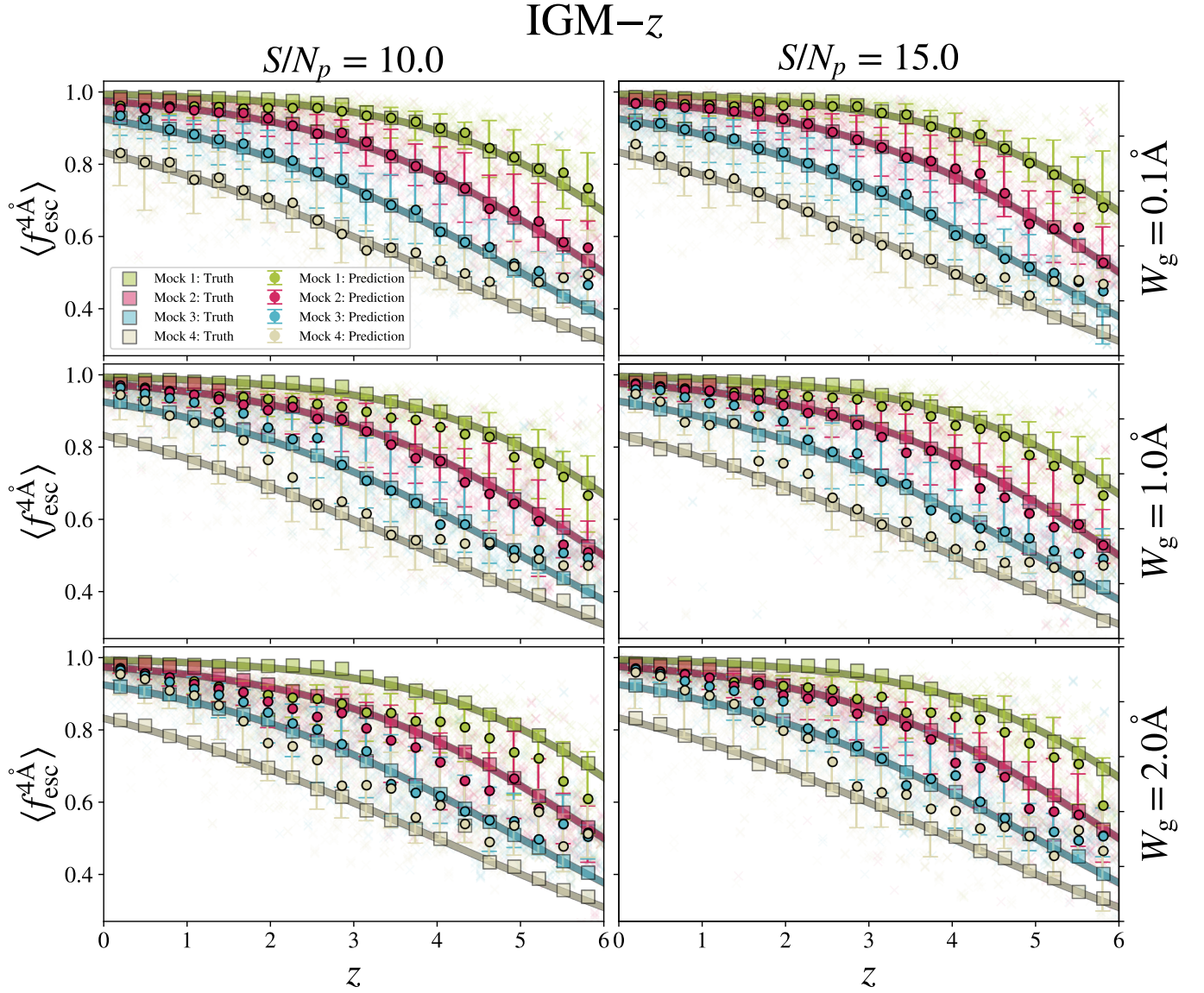


Fig. 9. Same as Fig. 8 but for the IGM+z model.

4.3. Stacked line profile reconstruction.

In this section, we explore zELDA's capability to reconstruct the stack of intrinsic Ly α line profiles. Our focus here is to study whether zELDA is able to measure the evolution or non-evolution of the intrinsic stacked Ly α line profile. For this goal, we used mock samples of the Ly α line profiles. Meanwhile, a detailed analysis for individual spectral recovery can be found in Appendix D.

Given a sample of Ly α line profiles with a given redshift distribution, we follow the next procedure. First, we run zELDA (IGM+z, IGM-z or NoIGM) in order to obtain the redshift of the Ly α line profile by running our ANN. Next, we move all observed Ly α line profiles to a common wavelength array in the rest frame using the redshift provided by zELDA. Every Ly α line profile is normalized so that their maximum reaches unity. Finally, the stacked Ly α line profile is computed as the median flux in each wavelength bin.

We present two types of samples of mock Ly α line profile. In the first one, Mock_Evo, the intrinsic Ly α line profiles change with redshift. In particular, for a given Ly α line profile at red-

shift z_i , the outflow properties are linearly interpolated from the z nodes listed in Tab.1. For illustration, in each node, the outflow parameter combination was chosen so that the intrinsic line profile changed dramatically from node to node. The top left panel of Fig. 10 shows the stacked Ly α line profile at redshift between 0.75 and 1.25 (grey), between 1.75 and 2.25 (blue), between 2.75 and 3.25 (green), between 3.75 and 4.25 (yellow) and between 4.75 and 5.25 (red).

In the second mock sample, Mock_fix, all the line profiles use the same outflow parameters: $V_{\text{exp}} = 200.0 \text{ km s}^{-1}$, $N_{\text{H}} = 19.3 \text{ cm}^{-2}$, $EW_{\text{in}} = 20.0 \text{ Å}$, $W_{\text{in}} = 2.0 \text{ Å}$ and $\tau_a = 0.001$. These were chosen so that the intrinsic line profile resembled the observed Ly α line profiles stack at low redshift (Hayes et al. 2023). The top left panel of Fig. 11 shows this outflow line profile.

The Mock_Evo observed stacked Ly α line profile after including the IGM is shown in the top right panels of Fig. 10 for two spectral quality combinations: $S/N_p = 15$ and $W_g = 0.1 \text{ Å}$ (top) and $S/N_p = 10$ and $W_g = 2.0 \text{ Å}$ (bottom). For both spectral quality configurations, the higher the redshift, the more attenuated the blue side of Ly α . Meanwhile, the red side of Ly α remains

Stacks: redshift invariant

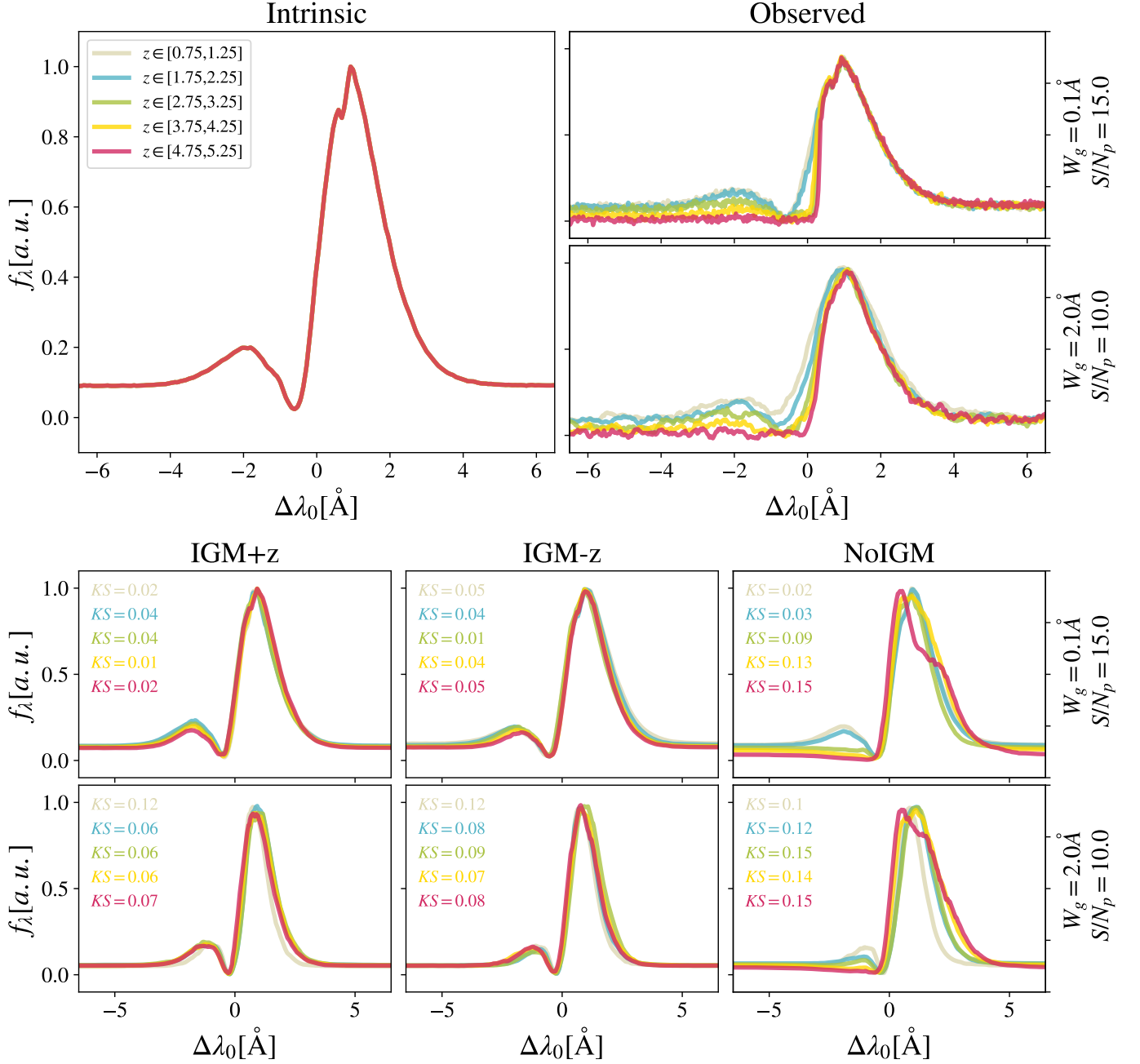


Fig. 11. Same as Fig. 10 but for the redshift invariant Ly α line profiles.

higher the redshift, the more absorbed is the blue side of Ly α . In particular, at $z \sim 4$ the blue peak is erased. In addition, spectral quality has an impact on the observed stack spectrum of Ly α . As W_g is fixed in the observed frame, the resolution element in rest frame is smaller for sources at higher redshift. This causes that, for $S/N_p = 10.0$, $W_g = 2.0 \text{ \AA}$, the Ly α stack spectrum at $z \sim 1$ is wider than at $z \sim 5$.

We present the results for the stacked Ly α line profile reconstruction in Fig. 10 for the redshift-dependent Ly α line profile (Mock_Evo). In order to compute the reconstructed intrinsic Ly α line profiles we run zELDA in each individual observed line profile. Next, we follow the same procedure for computing

the stacked line profile described earlier. The stacked Ly α line profile reconstructed by IGM+z, IGM-z and NoIGM are shown in the bottom columns from left to right. The top row shows $S/N_p = 15.0$, $W_g = 0.1 \text{ \AA}$ while the bottom shows $S/N_p = 10.0$, $W_g = 2.0 \text{ \AA}$. The accuracy of the reconstruction is quantified by the KS estimator between the intrinsic stack and the reconstructed one, shown within each panel.

In general, the three ANN models assess that there is a clear evolution in the Ly α stacked line profile. We find that, in general, IGM+z and IGM-z manage to reconstruct the intrinsic stacked Ly α line profile accurately with typical values below $KS = 0.1$. In particular, the stack is more accurate for the $S/N_p = 15.0$, W_g

$=0.1\text{\AA}$ configuration with typical $KS < 0.06$. For example, both IGM+z and IGM-z recover the blue peaks visible in the intrinsic stack at $z \sim 3, 4$ and 5 . Even the small hint of a blue peak present in the $z \sim 2$ bin is recovered. However, the reconstruction in the blue peaks is not perfect. For example, in the $z \sim 4$ stack, the reconstructed blue peak is slightly under predicted. It is also noticeable that the amplitude of the continuum blue side Ly α is relatively well recovered.

The NoIGM model recovers well the intrinsic Ly α line profile at $z \sim 1$, with $KS = 0.05$. However, at $z > 1$, the stack is poorly constrained with typical KS values greater than 0.1 . For example, the NoIGM ANN provides reconstructed Ly α line profiles that exhibit the same blue continuum as the observed stacked line profile. In addition, the blue peaks of the high-redshift bins were not recovered.

In Fig. 11 we show zELDA's prediction for the static Ly α line profile sample (Mock_fix). In general, we find the same trends as in Mock_Evo. Both the IGM+z and IGM-z models recover accurately the non-evolution of the stacked Ly α line profile. The stacked line profile is better reconstructed for better spectral quality. Typically $KS < 0.10$ for $S/N_p = 10.0$, $W_g = 2.0\text{\AA}$ and $KS < 0.05$ for $S/N_p = 15.0$, $W_g = 0.1\text{\AA}$. The blue peak is reconstructed at all redshifts, although with slightly different amplitudes. Meanwhile, NoIGM does not manage to recover the non-evolution. NoIGM predicts correctly the stacked line profile at $z \sim 1$ with $KS = 0.02$ for $S/N_p = 15.0$, $W_g = 0.1\text{\AA}$. However, at $z > 1.0$ does not recover the existence of the blue peak.

5. Summary and conclusions

The observed Ly α line profile is shaped by the complex radiative transfer taking place inside the galaxies in the interstellar medium, in the circumgalactic medium after escaping the galaxy and in the intergalactic medium. In this work, we have presented the second version of the open source code zELDA. zELDA's second version focuses on disentangling between the ISM and IGM contributions to the Ly α line profile using artificial neural networks. zELDA can be found at https://github.com/sidgl/zELDA_II along with installation and usage tutorials at <https://zelda-ii.readthedocs.io/index.html>.

Our training sets contain mock Ly α line profiles with ISM and IGM attenuation mimicking a wide range of observed spectral quality configurations. The ISM contributions come directly from the first version of zELDA ZP22, which counted with grid of precomputed 'shell model' line profiles using a Ly α Monte Carlo radiative transfer (LyART Orsi et al. 2012). Meanwhile, the IGM attenuation comes from the Ly α transmission curves published by Byrohl & Gronke (2020). These are obtained by running a Monte Carlo Ly α radiative transfer code (a modified version of ILTIS, Behrens et al. 2019) in the IllustrisTNG100 simulation (Nelson et al. 2019), at six snapshots between redshifts of 0.0 and 5.0 .

We have presented three ANN models. All include the first 100 components of the PCA decomposition of the observed Ly α line profile and spectral quality. First, IGM+z, includes a proxy redshift of the sources and the IGM transmission lines assigned to the sources in the training are at the redshift of the source. Meanwhile, IGM-z does not include the redshift of the source in the input and sources are assigned random IGM transmission curves. Finally, for comparison, NoIGM, which includes a proxy redshift of the source in the input but the Ly α line profiles in the training set lack the IGM contribution.

zELDA's performance on mock Ly α line profile can be summarized as follows:

- We have tested our ANN models in mock Ly α line profiles. We find that IGM+z and IGM-z manage to reconstruct the shape of the Ly α line profile emerging from the ISM. The accuracy of the reconstruction depends on the spectral quality of the observed line profile. For example, for the typical spectral quality of Ly α line profiles obtained by the Cosmic Origins Spectrograph (COS Green et al. 2012) on board the Hubble Space Telescope, 95% of the Ly α line profiles should be recovered with a Kolmogórov-Smirnov estimator below 0.1 . Meanwhile, for data with the spectral quality of the MUSE-WIDE survey Urrutia et al. (2019); Herenz et al. (2017), typically, 81% of the Ly α line profiles are reconstructed with a $KS < 0.1$.
- Additionally, we have tested zELDA's capabilities to reconstruct the stacked line profile of the line emerging from the ISM from the IGM attenuated line profiles. We find that the Ly α stacked line profile can be recovered with $KS < 0.7$ for HST and MUSE-like data by both IGM+z and IGM-z. Moreover, the precision in the stack reconstruction enables us to detect evolution or non-evolution in the ISM stacked line profile.
- Interestingly zELDA is capable of predicting the IGM Ly α escape fraction, $f_{\text{esc}}^{4\text{\AA}}$, with an uncertainty of ~ 0.03 in HST-like data and ~ 0.12 for MUSE-like data. In fact, we found that IGM+z and IGM-z are able to detect evolution in $f_{\text{esc}}^{4\text{\AA}}$ from redshift 2.0 onward for MUSE-like data. Meanwhile, IGM+z provides $f_{\text{esc}}^{4\text{\AA}}$ values biased towards 1 at $z < 1.0$. In contrast, IGM-z seems unbiased in this redshift range.

This work advances our modeling of the Ly α emission line and fitting by incorporating the IGM attenuation along the line of sight. zELDA's current version presents some limitations, like recovering $f_{\text{esc}}^{4\text{\AA}}$ at $f_{\text{esc}}^{4\text{\AA}} < 0.5$ or reconstructing the shape of Ly α line profiles with $f_{\text{esc}}^{4\text{\AA}} < 0.4$. Nevertheless, this work demonstrates that disentangling the ISM from the IGM a contributions is possible at the level of individual Ly α line profiles. This opens multiple scientific paths. Some examples of the many applications that zELDA can have in observed data are given below.

- The exploration of what shapes the ISM emerging Ly α line profiles in high-redshift galaxies. This could be done by correlating the inferred 'shell model' parameters with the luminosity of their spectral features or galaxy properties like mass, neutral hydrogen column density and so on.
- The current Ly α luminosity functions (LF) are measured with the observed Ly α luminosity, which is attenuated by the IGM. zELDA provides a $f_{\text{esc}}^{4\text{\AA}}$ source-by-source. Therefore, zELDA can provide the Ly α LF for star forming sources before the IGM attenuation. This could shed light on the cosmic star formation history at high redshift.
- There is still some debate on whether the IGM large scale properties affect the visibility of Ly α . A spectroscopic survey covering a large enough area and using zELDA could directly measure if there is an excess of clustering signal in $f_{\text{esc}}^{4\text{\AA}}$ with respect that of LAEs.

Acknowledgements. The authors acknowledge the financial support from the MICIU with funding from the European Union NextGenerationEU and Generalitat Valenciana in the call Programa de Planes Complementarios de I+D+i (PRTR 2022) Project (VAL-JPAS), reference ASFAE/2022/025. This

work is part of the research Project PID2023-149420NB-I00 funded by MICIU/AEI/10.13039/501100011033 and by ERDF/EU. This work is also supported by the project of excellence PROMETEO CIPROM/2023/21 of the Conselleria de Educación, Universidades y Empleo (Generalitat Valenciana). MG thanks the Max Planck Society for support through the Max Planck Research Group. DS acknowledges the support by the Tsinghua Shui Mu Scholarship, funding of the National Key R&D Program of China (grant no. 2023YFA1605600), the science research grants from the China Manned Space Project with no. CMS-CSST2021-A05, and the Tsinghua University Initiative Scientific Research Program (no. 20223080023). This research made use of matplotlib, a Python library for publication quality graphics (Hunter 2007), NumPy (Harris et al. 2020) and SciPy (Virtanen et al. 2020).

References

- Ahn, S. 2003, *Journal of Korean Astronomical Society*, 36, 145
- Behrens, C., Pallottini, A., Ferrara, A., Gallerani, S., & Vallini, L. 2019, *MNRAS*, 486, 2197
- Byrohl, C. & Gronke, M. 2020, *A&A*, 642, L16
- Byrohl, C., Nelson, D., Behrens, C., et al. 2021, *MNRAS*, 506, 5129
- Byrohl, C., Saito, S., & Behrens, C. 2019, *MNRAS*, 489, 3472
- Caruana, J., Wisotzki, L., Herenz, E. C., et al. 2020, *VizieR Online Data Catalog*, J/MNRAS/473/30
- Dijkstra, M., Haiman, Z., & Spaans, M. 2006, *ApJ*, 649, 14
- Farrow, D. J., Sánchez, A. G., Ciardullo, R., et al. 2021, *arXiv e-prints*, arXiv:2104.04613
- Faucher-Giguère, C.-A., Prochaska, J. X., Lidz, A., Hernquist, L., & Zaldarriaga, M. 2008, *ApJ*, 681, 831
- Green, J. C., Froning, C. S., Osterman, S., et al. 2012, *ApJ*, 744, 60
- Greene, J., Bezanson, R., Ouchi, M., Silverman, J., & the PFS Galaxy Evolution Working Group. 2022, *arXiv e-prints*, arXiv:2206.14908
- Gronke, M. 2017, *A&A*, 608, A139
- Gronke, M., Dijkstra, M., McCourt, M., & Oh, S. P. 2016, *ApJ*, 833, L26
- Gurung-López, S., Gronke, M., Saito, S., Bonoli, S., & Orsi, A. A. 2022, *MNRAS*, 510, 4525
- Gurung-López, S., Orsi, Á. A., & Bonoli, S. 2019a, *MNRAS*, 490, 733
- Gurung-López, S., Orsi, Á. A., Bonoli, S., Baugh, C. M., & Lacey, C. G. 2019b, *MNRAS*, 486, 1882
- Gurung-López, S., Orsi, Á. A., Bonoli, S., et al. 2020, *MNRAS*, 491, 3266
- Gurung-López, S., Saito, S., Baugh, C. M., et al. 2021a, *MNRAS*, 500, 603
- Gurung-López, S., Saito, S., Baugh, C. M., et al. 2021b, *MNRAS*, 500, 603
- Harris, C. R., Millman, K. J., van der Walt, S. J., et al. 2020, *Nature*, 585, 357
- Hayes, M. J., Runnholm, A., Scarlata, C., Gronke, M., & Rivera-Thorsen, T. E. 2023, *MNRAS*, 520, 5903
- Herenz, E. C., Urrutia, T., Wisotzki, L., et al. 2017, *A&A*, 606, A12
- Hill, G. J., Gebhardt, K., Komatsu, E., et al. 2008, in *Astronomical Society of the Pacific Conference Series*, Vol. 399, *Astronomical Society of the Pacific Conference Series*, ed. T. Kodama, T. Yamada, & K. Aoki, 115–+
- Hunter, J. D. 2007, *Computing In Science & Engineering*, 9, 90
- Kakuma, R., Ouchi, M., Harikane, Y., et al. 2019, *arXiv e-prints*, arXiv:1906.00173
- Laursen, P., Sommer-Larsen, J., & Razoumov, A. O. 2011, *ApJ*, 728, 52
- Marinacci, F., Vogelsberger, M., Pakmor, R., et al. 2018, *MNRAS*, 480, 5113
- Naiman, J. P., Pillepich, A., Springel, V., et al. 2018, *MNRAS*, 477, 1206
- Nelson, D., Springel, V., Pillepich, A., et al. 2019, *Computational Astrophysics and Cosmology*, 6, 2
- Neufeld, D. A. 1990, *ApJ*, 350, 216
- Orsi, A., Lacey, C. G., & Baugh, C. M. 2012, *MNRAS*, 425, 87
- Orsi, Á., Padilla, N., Groves, B., et al. 2014, *MNRAS*, 443, 799
- Ouchi, M., Harikane, Y., Shibuya, T., et al. 2018, *PASJ*, 70, S13
- Ouchi, M., Ono, Y., & Shibuya, T. 2020, *Annual Review of Astronomy and Astrophysics*, 58, 617
- Pillepich, A., Nelson, D., Hernquist, L., et al. 2018, *MNRAS*, 475, 648
- Rudie, G. C., Steidel, C. C., & Pettini, M. 2012, *ApJ*, 757, L30
- Runnholm, A., Gronke, M., & Hayes, M. 2021, *PASP*, 133, 034507
- Schaerer, D., Hayes, M., Verhamme, A., & Teyssier, R. 2011, *A&A*, 531, A12
- Spinoso, D., Orsi, A., López-Sanjuan, C., et al. 2020, *A&A*, 643, A149
- Springel, V., Pakmor, R., Pillepich, A., et al. 2018, *MNRAS*, 475, 676
- Steidel, C. C., Erb, D. K., Shapley, A. E., et al. 2010, *ApJ*, 717, 289
- Torralba-Torregrosa, A., Gurung-López, S., Arnalte-Mur, P., et al. 2023, *A&A*, 680, A14
- Torralba-Torregrosa, A., Renard, P., Spinoso, D., et al. 2024, *A&A*, 690, A388
- Urrutia, T., Wisotzki, L., Kerutt, J., et al. 2019, *A&A*, 624, A141
- Verhamme, A., Garel, T., Ventou, E., et al. 2018, *MNRAS*, 478, L60
- Verhamme, A., Schaerer, D., Atek, H., & Tapken, C. 2007, in *Astronomical Society of the Pacific Conference Series*, Vol. 380, *Deepest Astronomical Surveys*, ed. J. Afonso, H. C. Ferguson, B. Mobasher, & R. Norris, 97
- Virtanen, P., Gommers, R., Oliphant, T. E., et al. 2020, *Nature Methods*, 17, 261
- Weiss, L. H., Bowman, W. P., Ciardullo, R., et al. 2021, *ApJ*, 912, 100
- Zheng, Z., Cen, R., Trac, H., & Miralda-Escudé, J. 2011, *ApJ*, 726, 38

Appendix A: Feature importance analysis.

The feature importance analysis of the spectral features is made by shuffling the fluxes in wavelength bins of 1\AA in the rest frame of the sources, as in ZP22. Next, we convert the altered spectrum with the PCA model and pass it to the ANN along with the actual W_g , $\Delta\lambda_{\text{pix}}$ and z_{max} values. Then, in order to compute the importance of W_g , $\Delta\lambda_{\text{pix}}$ and z_{max} , we shuffled these properties one by one. The importance is computed as $I = \sigma_{\text{original}}/\sigma_{\text{shuffled}} - 1$, where σ_{original} is the accuracy of the ANN predicting a given output variable and σ_{shuffled} is that but using the perturbed input. In general, $\sigma_{\text{shuffled}} < \sigma_{\text{original}}$, since the input without perturbation contains more information. Therefore, $I > 0$, in general.

In Fig. A.1 we show the feature importance analysis of $\Delta\lambda_{\text{True}}$, V_{exp} , N_{H} , EW_{in} , W_{in} and $f_{\text{esc}}^{4\text{\AA}}$ for the IGM+z model with $W_g = 0.25\text{\AA}$, $\Delta\lambda_{\text{pix}} = 0.125\text{\AA}$ and $S/N_p = 15.0$. The general trends found here are also present for other quality configurations and IGM-z and NoIGM. We find the same general trends as in ZP22. For $\Delta\lambda_{\text{True}}$, V_{exp} , N_{H} , W_{in} and $f_{\text{esc}}^{4\text{\AA}}$ the regions closer than 5\AA contains the most information. This tends to be skewed redwards $\text{Ly}\alpha$ in the three models. However, the models including IGM, IGM+z and IGM-z, give more importance to redder wavelengths than NoIGM. This shows that IGM+z and IGM-z 'trust' more the red side of $\text{Ly}\alpha$. This makes sense considering that the blue side of $\text{Ly}\alpha$ could be heavily influence by the IGM. Still, some information in the blue side is being used in order to estimate the output. The ANN constraining EW_{in} gives the most importance to the region $+5\text{\AA}$ from $\text{Ly}\alpha$, which should be dominated by the continuum of the source. In particular, the ANN constraining $\Delta\lambda_{\text{True}}$ exhibits the narrowest importance peak around $\text{Ly}\alpha$ ($\pm 1\text{\AA}$). Finally, focusing in $f_{\text{esc}}^{4\text{\AA}}$, we find that in the IGM+z model, the importance of z_{max} is 0.38, which shows that it plays a significant role in determining $f_{\text{esc}}^{4\text{\AA}}$. Actually, $f_{\text{esc}}^{4\text{\AA}}$ is variable for which z_{max} is the most informative.

Appendix B: Individual parameters uncertainty estimation

In ZP22 we found that the uncertainty computed through this methodology had less than a 10% error, and therefore needed no correction. However, we find that the models presented in this work tend to underestimate the uncertainty in the output parameters. In the top panels of Fig. B.1 we show the comparison between the fraction of cases that a measurement is in compatible with the intrinsic true value, f_{comp} , as a function of the confidence level. Each subplot shows the indicated outflow property. Ideally this relation should follow perfectly a 1:1 trend. Focusing in NoIGM (yellow) we find that before correction (solid line) the uncertainty is underestimated no more than 10%, except for τ_a , as it was the case in ZP22, which did not include IGM. We find that the uncertainty in the outflow parameters can be underestimated up a 20% in IGM+z and IGM-z. This bias in the uncertainty estimation is produced by the IGM inclusion. Some IGM transmission curve can produce observed $\text{Ly}\alpha$ line really close to unabsorbed thin shell spectrum. In some of these cases the outflow parameters predicted correspond to the 'fake' thin shell spectrum rather than the intrinsic one. This causes than in smaller fraction of cases the true outflow parameters and the predicted ones are compatible at a given confidence level than in NoIGM. We correct our uncertainty estimation so that f_{comp} and the confidence level follow a 1:1 relation. The correction factors depend on the confidence level and are shown in the bottom pan-

els. f_{comp} as a function of the confidence level after the correction is shown in dots.

Appendix C: Accuracy of individual parameters

As described in ZP22, the accuracy of the ANN models on the outflow parameters and redshift depend on the quality of the observed spectrum. In general, spectrum with better quality will be better reconstructed by our ANN models.

Individual cases of how the observed line profile quality changes the reconstructed line profile is shown in Fig. 3. Each row shows the same intrinsic line and IGM absorption at different qualities (better to worse from left to right) and the true and predicted outflow parameters and IGM escape fraction are listed in Tab.C.1. In general, for sources of the best quality (A, D and G) the predicted parameters for IGM+z and IGM-z are 1σ compatible with the true values. However as the observed line profile becomes noisier and less resolved the accuracy in the parameters decreases. For example, in the middle row, for the best quality (D) the amplitude of the blue peak is reasonably well reconstructed and $\text{KS}=0.04$. Meanwhile, for the lowest quality (F), $\text{KS}=0.09$ and the positions and amplitude of the blue peak are slightly miss-predicted.

In order to quantify the accuracy of IGM+z or IGM-z and NoIGM we computed 10000 line profiles with IGM absorption between redshift 0 and 6 for 24 combinations of quality (4 for S/N_p and 6 for W_g). In Fig. C.1, C.2 and C.3 we show the accuracy for the output parameters of IGM+z, IGM-z and NoIGM, respectively. In general, we find that IGM+z and IGM-z exhibit the same accuracy across $f_{\text{esc}}^{4\text{\AA}}$ and spectral quality for all properties. Also, the accuracy of all the output parameters decreases with the line profile quality. Worse $\text{Ly}\alpha$ line profiles (larger W_g and smaller S/N_p) are recovered with worse redshift, outflow parameters and $f_{\text{esc}}^{4\text{\AA}}$. This happens at every $f_{\text{esc}}^{4\text{\AA}}$ interval.

Focusing in the range $f_{\text{esc}}^{4\text{\AA}} \in [0.95, 1.0]$, we find NoIGM actually performs better than IGM+z and IGM-z. For example, at $W_g = 0.1$ and $S/N_p = 15.0$, the accuracy of NoIGM is better than that of IGM+z and IGM-z for redshift, V_{exp} , N_{H} and W_{in} (a $\sim 10\%$). This shows that when the $\text{Ly}\alpha$ line profiles is mostly unabsorbed by the IGM the NoIGM works better than IGM+z or IGM-z. This is due to the fact that NoIGM is trained only with IGM free $\text{Ly}\alpha$ line profiles. In comparison, IGM+z or IGM-z are trained with a much more diverse $\text{Ly}\alpha$ line profile population. This can be a consequence of the outflow parameters confusion discussed in 4. A small fraction of $\text{Ly}\alpha$ line profiles with $f_{\text{esc}}^{4\text{\AA}} \sim 1.0$ are reconstructed as if they were more absorbed than what they actually are, lowering the accuracy in the outflow parameters and redshift.

Meanwhile, IGM+z and IGM-z outperform NoIGM when $f_{\text{esc}}^{4\text{\AA}} < 0.95$. In general the accuracy for all the output parameters decreases with the true $f_{\text{esc}}^{4\text{\AA}}$. This is due to the fact that, at smaller values of $f_{\text{esc}}^{4\text{\AA}}$ more information has been destroyed by the IGM. However, NoIGM's accuracy drops fast with decreasing $f_{\text{esc}}^{4\text{\AA}}$, while they accuracy IGM+z and IGM-z goes down slowly.

For instance, focusing on $W_g = 0.1$ and $S/N_p = 15.0$, the accuracy in V_{exp} at $f_{\text{esc}}^{4\text{\AA}} \in [0.95, 1.0]$ for NoIGM is 0.11 km s^{-1} , while at $f_{\text{esc}}^{4\text{\AA}} \in [0.8, 0.95]$ it drops to 0.35 km s^{-1} , at $f_{\text{esc}}^{4\text{\AA}} \in [0.65, 0.8]$ it drops to 0.64 km s^{-1} . Meanwhile, for IGM+z (IGM-z), the V_{exp} $f_{\text{esc}}^{4\text{\AA}} \in [0.95, 1.0]$ is 0.17 km s^{-1} (0.14 km s^{-1}), while at $f_{\text{esc}}^{4\text{\AA}} \in [0.8, 0.95]$ it is 0.20 km s^{-1} (0.19 km s^{-1}), at $f_{\text{esc}}^{4\text{\AA}} \in [0.65, 0.8]$ it is 0.3 km s^{-1} (0.23 km s^{-1}). This same trend is also found at other

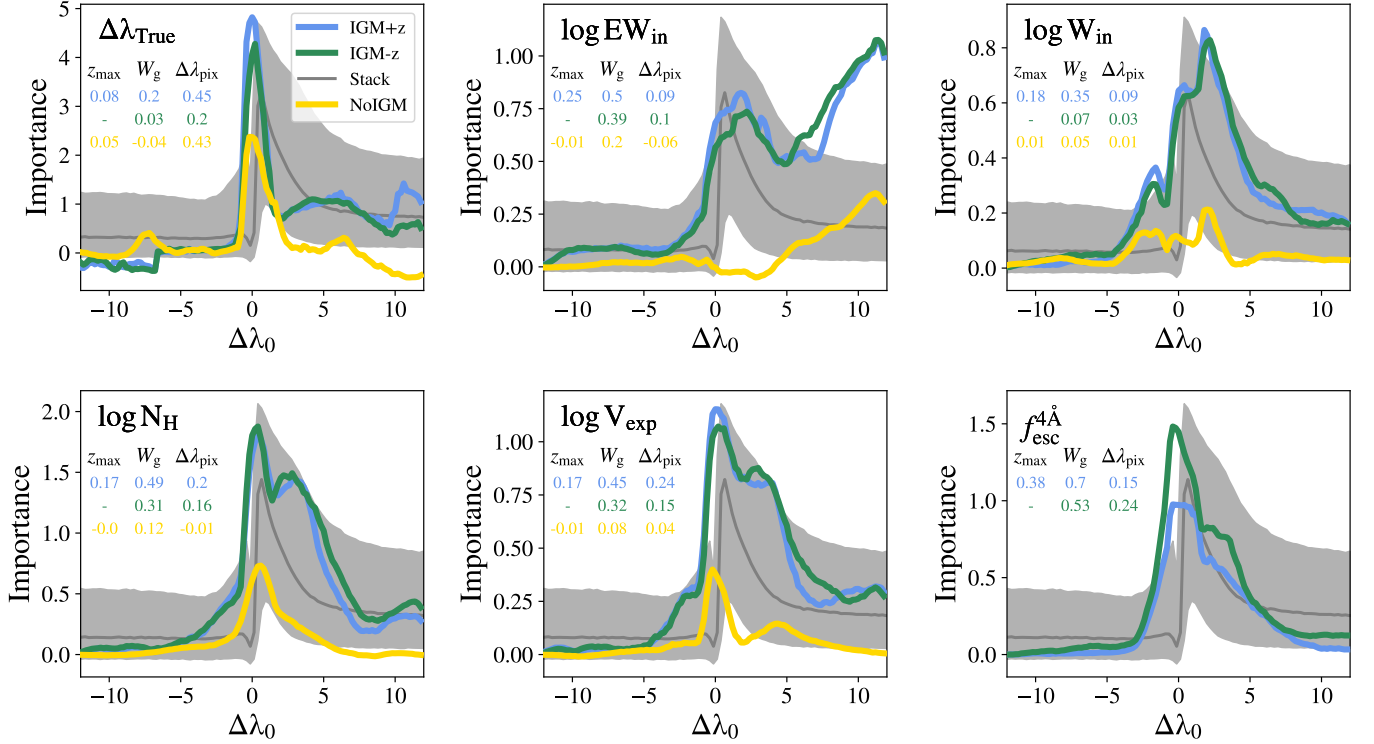


Fig. A.1. Feature importance analysis for the IGM+z (blue), IGM-z (green) and NoIGM (yellow). For comparison, the stacked line profiles with its 1σ scatter is shown in grey. Each subplot shows the importance determining a different property. In top row, $\Delta\lambda_{\text{True}}$, EW_{in} , W_{in} from left to right. In the bottom row, N_{H} , V_{exp} , $f_{\text{esc}}^{4\text{\AA}}$ from left to right. In each subplot we also show the z_{\max} , W_g and $\Delta\lambda_{\text{pix}}$ importance for each model in its matching color in the small table.

spectral quality configurations for N_{H} , EW_{in} and τ_a (although τ_a is not displayed).

We find that the accuracy in the accuracy in Ly α wavelength follows a different trend. While it is true that in NoIGM it drops fast for decreasing $f_{\text{esc}}^{4\text{\AA}}$ values, we find that for IGM+z and IGM-z it initially drops and then stabilizes at intermediate $f_{\text{esc}}^{4\text{\AA}}$ values ($f_{\text{esc}}^{4\text{\AA}} \in [0.3, 0.8]$) before rising again at $f_{\text{esc}}^{4\text{\AA}} \sim 0.3$. focusing on $W_g = 0.1$ and $S/N_p = 15.0$, $f_{\text{esc}}^{4\text{\AA}} \in [0.95, 1.0]$ for NoIGM is 0.21\AA , while at $f_{\text{esc}}^{4\text{\AA}} \in [0.8, 0.95]$ it drops to 0.75\AA , at $f_{\text{esc}}^{4\text{\AA}} \in [0.65, 0.8]$ it drops to 1.5\AA , and at $f_{\text{esc}}^{4\text{\AA}} \in [0.5, 0.65]$ up to 2.0\AA . Meanwhile, for IGM+z (IGM-z), the Ly α wavelength rest frame accuracy at $f_{\text{esc}}^{4\text{\AA}} \in [0.95, 1.0]$ is 0.28\AA (0.24\AA), while at $f_{\text{esc}}^{4\text{\AA}} \in [0.8, 0.95]$ it is 0.26\AA (0.3\AA), at $f_{\text{esc}}^{4\text{\AA}} \in [0.65, 0.8]$ it is 0.25\AA (0.20\AA), and at $f_{\text{esc}}^{4\text{\AA}} \in [0.5, 0.65]$ up to 0.23\AA (0.18\AA). This is also found at other spectral quality configurations. While at lower values of $f_{\text{esc}}^{4\text{\AA}}$, more outflow information is erased by the IGM, it is also true that more IGM information is imprinted on the Ly α line profile. The addition of this information, such as the position of a sudden flux drop (e.g. cases *S* and *T* of Fig. 6), enhances the accuracy redshift of the source.

Regarding the accuracy on $f_{\text{esc}}^{4\text{\AA}}$ we find that both, IGM+z and IGM-z, are able to give accurate prediction for $f_{\text{esc}}^{4\text{\AA}}$ in a wide range of spectral quality and in a broad $f_{\text{esc}}^{4\text{\AA}}$ regime. As for the outflow properties, we find that the $f_{\text{esc}}^{4\text{\AA}}$ accuracy decreases for more absorbed Ly α line profiles (smaller $f_{\text{esc}}^{4\text{\AA}}$). In the best case scenario considered ($W_g = 0.1$ and $S/N_p = 15.0$), the $f_{\text{esc}}^{4\text{\AA}}$ accuracy of IGM+z (IGM-z) is 0.05 (0.03) at $f_{\text{esc}}^{4\text{\AA}} \sim 1$, 0.06 (0.06) at $f_{\text{esc}}^{4\text{\AA}} \sim 0.87$, 0.09 (0.09) at $f_{\text{esc}}^{4\text{\AA}} \sim 0.72$, 0.12 (0.08) at $f_{\text{esc}}^{4\text{\AA}} \sim 0.62$

and 0.14 (0.09) at $f_{\text{esc}}^{4\text{\AA}} \sim 0.42$. Remarkable, $f_{\text{esc}}^{4\text{\AA}}$ is relatively well estimated also for Ly α line profiles with worse quality. The $f_{\text{esc}}^{4\text{\AA}}$ uncertainty in the IGM-z is below 0.15 , in general, even for $W_g = 4.0\text{\AA}$ and $S/N_p = 5.0$.

Comparing to the previous zELDA ANN presented in ZP22 (Their Fig.8), IGM+z, IGM-z and NoIGM present the same or slightly better accuracy at the $f_{\text{esc}}^{4\text{\AA}} \in [0.95, 1.0]$ regime. In Gurung-López et al. (2022) no IGM features were included, so the most direct comparison would be NoIGM with the their model. For instance, the NoIGM redshift accuracy for the best scenario in both works ($W_g = 0.1$ and $S/N_p = 15.0$) is 0.21\AA , while theirs was 0.26\AA . The V_{exp} NoIGM accuracy is 0.11 km s^{-1} while theirs was 0.14 km s^{-1} . Meanwhile, τ_a , EW_{in} and W_{in} exhibit the almost the same accuracy in ZP22 and here. NoIGM is only a $\sim 10\%$ better for these output properties. This increase in accuracy is due to the different ANN configuration and the changes in the input.

Appendix D: Accuracy in the shape of line profile reconstruction

In this section we study the accuracy in the shape of the recovered intrinsic Ly α line profile. Fig. D.1 shows the KS distribution for three mocks made in the same methodology as those for the parameter accuracy (Sect. C). In particular, $S/N_p = 15.0$ and $W_g = 0.25\text{\AA}$, $S/N_p = 10.0$ and $W_g = 0.5\text{\AA}$ and $S/N_p = 7.5$ and $W_g = 1.0\text{\AA}$ are shown from left to right. The KS distribution of the predicted Ly α line profiles by IGM+z, IGM-z and NoIGM are shown in blue, green and yellow, respectively. The horizontal dashed lines indicate the median of each distribution. In general,

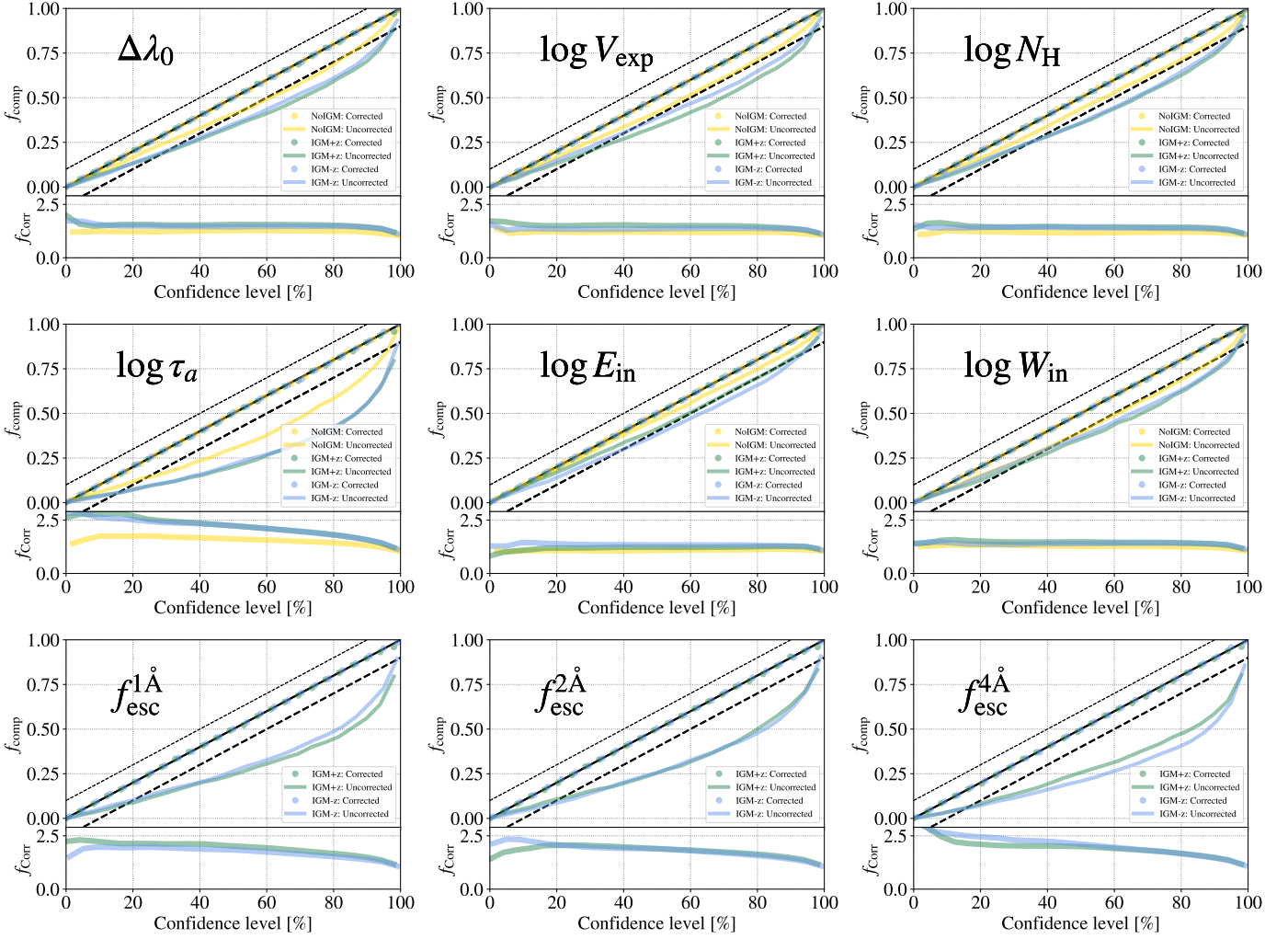


Fig. B.1. Top: Comparison between the fraction of cases that a measurement is in agreement with the intrinsic true value, f_{comp} , as a function of the confidence level. Bottom: Applied correction factor to uncertainty. The uncorrected f_{comp} is shown in colored solid lines, which IGM+z in green, IGM-z in blue and NoIGM in yellow. f_{comp} after the correction is shown in colored dots. In each panel a different output property is shown. In the first row z_{max} , V_{exp} and N_{H} from left to right. In the second row τ_a , E_{in} , W_{in} , from left to right. In the third row $f_{\text{esc}}^{1\text{\AA}}$, $f_{\text{esc}}^{2\text{\AA}}$, and $f_{\text{esc}}^{4\text{\AA}}$ from left to right. The diagonal black dashed lines show the $1:1 \pm 10\%$ relation. Computed using 10^4 line profiles with quality $W_{\text{g}} = 0.5\text{\AA}$, $\Delta\lambda_{\text{pix}} = 0.1\text{\AA}$ and $S/N_p = 10$.

we find that IGM+z and IGM-z outperform NoIGM. While there is a significant difference between the accuracy of IGM+z and IGM-z and NoIGM, IGM-z performs slightly better than IGM+z. IGM+z and IGM-z show a median value around $10^{-1.5}$ while the median KS value of NoIGM is around $10^{-1.2}$.

In Fig. D.2 we show the median of the KS distribution for the Ly α line profile mocks shown in Sect. C as a function of $f_{\text{esc}}^{4\text{\AA}}$ and for IGM+z, IGM-z and NoIGM, from left to right. As expected, the Ly α line profile shape are better recover at better spectral quality configurations. As for the outflow parameters, we find that NoIGM outperforms IGM+z and IGM-z in the $f_{\text{esc}}^{4\text{\AA}} \in [0.95, 1.0]$ regime. Also, the line profile accuracy of NoIGM drops fast with $f_{\text{esc}}^{4\text{\AA}}$. In the best scenario ($W_{\text{g}} = 0.1$ and $S/N_p = 15.0$), at $f_{\text{esc}}^{4\text{\AA}} \in [0.95, 1.0]$, the median KS is 0.01, at $f_{\text{esc}}^{4\text{\AA}} \in [0.8, 0.95]$ is 0.04 and at $f_{\text{esc}}^{4\text{\AA}} \in [0.35, 0.5]$ is 0.13. Meanwhile, IGM+z and IGM-z Ly α line profile reconstruction is better than that of NoIGM for $f_{\text{esc}}^{4\text{\AA}} < 0.95$. In particular, for IGM+z and IGM-z the median KS is generally below 0.05 in all the quality configurations explored.

Although for $W_{\text{g}} = 4.0\text{\AA}$ and small $f_{\text{esc}}^{4\text{\AA}}$ values, the median KS goes up to 0.9.

In Sect. 4 we show that in some cases and outflow configuration after passing through the IGM might resembles another outflow configuration. This causes confusion when reconstructing the Ly α lines (see examples in Fig. 7). In order to quantify the fraction of cases in which our ANN models reconstruct properly the Ly α we show in Fig. D.3 the percentile at which KS=0.1. In general, reconstructed Ly α line profiles with KS=0.1 are correctly recovered. Although in some cases Ly α lines with KS>0.1 are properly recovered (and vice versa), the KS=0.1 threshold is in general valid. We find the same general trends for smaller KS thresholds like 0.08.

As expected, the percentile at which KS=0.1 ($Q(KS = 0.1)$) depends on the Ly α line profile quality. The better the spectral quality, the higher the $Q(KS = 0.1)$ is. As before, NoIGM outperforms IGM+z and IGM-z in the unabsorbed regime, being $Q(KS = 0.1) = 98\%$, 0.96% and 0.96% respectively at the best configuration. However, IGM+z and IGM-z outperform NoIGM when $f_{\text{esc}}^{4\text{\AA}} < 0.95$. Remarkably $Q(KS = 0.1)$ is greater than the

$\sigma(\Delta\lambda_0[\text{\AA}]), z \in [0.0, 6.0]$							
f_{esc}	S/N _p	W_g	W_g	W_g	W_g	W_g	W_g
		0.1 \AA	0.25 \AA	0.5 \AA	1.0 \AA	2.0 \AA	4.0 \AA
[0.95, 1.0]	15.0	0.28	0.32	0.34	0.42	0.5	0.7
	10.0	0.36	0.35	0.38	0.48	0.67	0.87
	7.5	0.37	0.43	0.47	0.61	0.72	1.12
	5.0	0.53	0.54	0.71	0.9	1.15	1.36
[0.8, 0.95]	15.0	0.26	0.26	0.29	0.38	0.48	0.7
	10.0	0.27	0.3	0.35	0.41	0.61	0.87
	7.5	0.31	0.35	0.45	0.56	0.68	1.02
	5.0	0.42	0.51	0.65	0.84	1.1	1.56
[0.65, 0.8]	15.0	0.25	0.23	0.27	0.31	0.44	0.65
	10.0	0.23	0.25	0.26	0.36	0.46	0.87
	7.5	0.25	0.27	0.34	0.43	0.57	1.02
	5.0	0.34	0.42	0.59	0.69	1.0	1.54
[0.5, 0.65]	15.0	0.23	0.21	0.25	0.27	0.41	0.88
	10.0	0.21	0.22	0.24	0.3	0.54	1.0
	7.5	0.24	0.27	0.29	0.31	0.69	1.25
	5.0	0.34	0.46	0.7	0.85	1.34	1.98
[0.35, 0.5]	15.0	0.23	0.23	0.25	0.23	0.57	0.93
	10.0	0.35	0.25	0.22	0.34	0.45	1.2
	7.5	0.2	0.29	0.28	0.46	0.82	1.33
	5.0	0.47	0.77	0.69	0.91	1.32	2.07
[0.2, 0.35]	15.0	0.38	0.31	0.32	0.31	0.52	1.34
	10.0	0.25	0.3	0.36	0.37	0.62	1.3
	7.5	0.26	0.31	0.44	0.47	0.88	1.49
	5.0	0.47	0.75	0.92	1.31	1.67	2.24

$\sigma(\log V_{\text{exp}}[\text{km/s}], z \in [0.0, 6.0])$							
f_{esc}	S/N _p	W_g	W_g	W_g	W_g	W_g	W_g
		0.1 \AA	0.25 \AA	0.5 \AA	1.0 \AA	2.0 \AA	4.0 \AA
[0.95, 1.0]	15.0	0.17	0.18	0.2	0.26	0.31	0.38
	10.0	0.21	0.21	0.24	0.3	0.35	0.4
	7.5	0.23	0.24	0.28	0.32	0.38	0.42
	5.0	0.3	0.32	0.35	0.39	0.44	0.47
[0.8, 0.95]	15.0	0.2	0.21	0.23	0.3	0.35	0.42
	10.0	0.22	0.24	0.28	0.33	0.4	0.44
	7.5	0.25	0.28	0.31	0.38	0.42	0.46
	5.0	0.33	0.36	0.4	0.44	0.47	0.49
[0.65, 0.8]	15.0	0.3	0.3	0.36	0.4	0.47	0.5
	10.0	0.31	0.35	0.39	0.44	0.49	0.53
	7.5	0.33	0.38	0.43	0.48	0.51	0.54
	5.0	0.4	0.46	0.49	0.52	0.54	0.56
[0.5, 0.65]	15.0	0.38	0.42	0.44	0.49	0.54	0.57
	10.0	0.41	0.44	0.47	0.53	0.56	0.58
	7.5	0.43	0.48	0.52	0.54	0.57	0.6
	5.0	0.51	0.53	0.55	0.58	0.59	0.61
[0.35, 0.5]	15.0	0.44	0.5	0.54	0.56	0.58	0.57
	10.0	0.51	0.52	0.56	0.58	0.59	0.6
	7.5	0.52	0.54	0.54	0.58	0.58	0.6
	5.0	0.56	0.59	0.6	0.6	0.61	0.61
[0.2, 0.35]	15.0	0.53	0.53	0.58	0.55	0.58	0.59
	10.0	0.52	0.56	0.59	0.59	0.6	0.6
	7.5	0.59	0.59	0.61	0.6	0.59	0.6
	5.0	0.56	0.6	0.61	0.62	0.6	0.61

$\sigma(\log N_{\text{H}}[\text{cm}^{-2}], z \in [0.0, 6.0])$							
f_{esc}	S/N _p	W_g	W_g	W_g	W_g	W_g	W_g
		0.1 \AA	0.25 \AA	0.5 \AA	1.0 \AA	2.0 \AA	4.0 \AA
[0.95, 1.0]	15.0	0.32	0.38	0.4	0.49	0.58	0.73
	10.0	0.39	0.41	0.45	0.56	0.71	0.8
	7.5	0.43	0.48	0.55	0.63	0.76	0.9
	5.0	0.58	0.61	0.66	0.82	0.9	1.0
[0.8, 0.95]	15.0	0.37	0.38	0.45	0.51	0.61	0.73
	10.0	0.39	0.45	0.48	0.57	0.69	0.84
	7.5	0.46	0.5	0.54	0.67	0.76	0.91
	5.0	0.54	0.64	0.7	0.82	0.92	1.07
[0.65, 0.8]	15.0	0.47	0.47	0.56	0.59	0.72	0.83
	10.0	0.46	0.54	0.57	0.65	0.77	0.9
	7.5	0.51	0.54	0.62	0.7	0.8	0.96
	5.0	0.59	0.66	0.74	0.84	0.98	1.05
[0.5, 0.65]	15.0	0.61	0.63	0.67	0.75	0.79	0.86
	10.0	0.63	0.66	0.7	0.75	0.83	0.91
	7.5	0.65	0.69	0.71	0.76	0.85	0.9
	5.0	0.69	0.73	0.77	0.83	0.93	0.97
[0.35, 0.5]	15.0	0.7	0.72	0.74	0.74	0.81	0.83
	10.0	0.74	0.73	0.77	0.78	0.83	0.85
	7.5	0.71	0.71	0.75	0.81	0.81	0.83
	5.0	0.77	0.77	0.79	0.79	0.81	0.89
[0.2, 0.35]	15.0	0.69	0.76	0.79	0.78	0.76	0.84
	10.0	0.73	0.75	0.77	0.81	0.83	0.87
	7.5	0.74	0.73	0.77	0.8	0.84	0.85
	5.0	0.81	0.75	0.77	0.83	0.83	0.94

$\sigma(\log EW_{\text{in}}[\text{\AA}]), z \in [0.0, 6.0]$							
f_{esc}	S/N _p	W_g	W_g	W_g	W_g	W_g	W_g
		0.1 \AA	0.25 \AA	0.5 \AA	1.0 \AA	2.0 \AA	4.0 \AA
[0.95, 1.0]	15.0	0.14	0.13	0.15	0.15	0.17	0.19
	10.0	0.14	0.15	0.17	0.18	0.2	0.22
	7.5	0.15	0.17	0.18	0.2	0.22	0.24
	5.0	0.19	0.2	0.22	0.25	0.27	0.3
[0.8, 0.95]	15.0	0.14	0.14	0.15	0.16	0.17	0.18
	10.0	0.15	0.15	0.16	0.18	0.19	0.21
	7.5	0.15	0.17	0.17	0.2	0.22	0.24
	5.0	0.18	0.2	0.22	0.25	0.28	0.31
[0.65, 0.8]	15.0	0.15	0.16	0.17	0.18	0.19	0.18
	10.0	0.16	0.17	0.17	0.2	0.21	0.22
	7.5	0.17	0.18	0.19	0.21	0.23	0.26
	5.0	0.2	0.21	0.23	0.25	0.28	0.31
[0.5, 0.65]	15.0	0.15	0.15	0.16	0.17	0.18	0.19
	10.0	0.15	0.16	0.17	0.19	0.2	0.21
	7.5	0.17	0.18	0.19	0.21	0.21	0.22
	5.0	0.19	0.21	0.22	0.24	0.25	0.28
[0.35, 0.5]	15.0	0.14	0.15	0.15	0.16	0.17	0.19
	10.0	0.16	0.15	0.16	0.17	0.18	0.2
	7.5	0.16	0.17	0.17	0.17	0.19	0.21
	5.0	0.18	0.19	0.2	0.22	0.23	0.24
[0.2, 0.35]	15.0	0.19	0.17	0.18	0.19	0.2	0.2
	10.0	0.18	0.19	0.19	0.2	0.21	0.23
	7.5	0.18	0.18	0.19	0.2	0.21	0.23
	5.0	0.19	0.2	0.21	0.21	0.23	0.25

$\sigma(\log W_{\text{in}}[\text{\AA}]), z \in [0.0, 6.0]$							
f_{esc}	S/N _p	W_g	W_g	W_g	W_g	W_g	W_g
		0.1 \AA	0.25 \AA	0.5 \AA	1.0 \AA	2.0 \AA	4.0 \AA
[0.95, 1.0]	15.0	0.3	0.3	0.32	0.33	0.37	0.39
	10.0	0.32	0.32	0.33	0.36	0.39	0.41
	7.5	0.33	0.35	0.35	0.38	0.4	0.43
	5.0	0.36	0.38	0.41	0.43	0.43	0.44
[0.8, 0.95]	15.0	0.3	0.3	0.31	0.33	0.35	0.38
	10.0	0.31	0.3	0.33	0.35	0.38	0.41
	7.5	0.31	0.33	0.36	0.37	0.4	0.42
	5.0	0.35	0.37	0.39	0.41	0.44	0.45
[0.65, 0.8]	15.0	0.28	0.29	0.32	0.33	0.37	0.39
	10.0	0.3	0.31	0.34	0.35	0.38	0.42
	7.5	0.32	0.35	0.36	0.38	0.41	0.43
	5.0	0.36	0.37	0.4	0.42	0.42	0.45
[0.5, 0.65]	15.0	0.28	0.29	0.33	0.34	0.37	0.41
	10.0	0.3	0.31	0.34	0.34	0.38	0.42
	7.5	0.31	0.33	0.36	0.37	0.39	0.44
	5.0	0.36	0.36	0.39	0.42	0.43	0.45
[0.35, 0.5]	15.0	0.26	0.26	0.31	0.32	0.37	0.4
	10.0	0.29	0.3	0.32	0.35	0.38	0.42
	7.5	0.3	0.33	0.34	0.37	0.39	0.45
	5.0	0.35	0.37	0.38	0.42	0.42	0.46
[0.2, 0.35]	15.0	0.27	0.29	0.31	0.32	0.36	0.38
	10.0	0.28	0.28	0.31	0.36	0.39	0.42
	7.5	0.29	0.32	0.33	0.38	0.4	0.44
	5.0	0.35	0.36	0.37	0.42	0.42	0.45

$\sigma(f_{\text{GM}}^{\text{4\AA}}), z \in [0.0, 6.0]$							
f_{esc}	S/N _p	W_g	W_g	W_g	W_g	W_g	W_g
		0.1 \AA	0.25 \AA	0.5 \AA	1.0 \AA	2.0 \AA	4.0 \AA
[0.95, 1.0]	15.0	0.05	0.05	0.05	0.06	0.06	0.08
	10.0	0.05	0.05	0.06	0.07	0.08	0.09
	7.5	0.05	0.06	0.06	0.08	0.09	0.1
	5.0	0.06	0.07	0.08	0.1	0.11	0.12
[0.8, 0.95]	15.0	0.06	0.06	0.07	0.07	0.08	0.09
	10.0	0.06	0.07	0.07	0.08	0.09	0.1
	7.5	0.07	0.07	0.08	0.09	0.1	0.11
	5.0	0.07	0.08	0.1	0.11	0.12	0.13
[0.65, 0.8]	15.0	0.09	0.1	0.1	0.11	0.12	0.12
	10.0	0.09	0.1	0.11	0.12	0.12	0.13
	7.5	0.09	0.1	0.11	0.12	0.12	0.13
	5.0	0.1	0.11	0.12	0.13	0.14	0.14
[0.5, 0.65]	15.0	0.1	0.1	0.12	0.14	0.15	0.15
	10.0	0.1	0.11	0.13	0.14	0.14	0.15
	7.5	0.1	0.12	0.13	0.14	0.14	0.14
	5.0	0.12	0.13	0.14	0.15	0.15	0.15
[0.35, 0.5]	15.0	0.11	0.11	0.13	0.15	0.17	0.17
	10.0	0.11	0.13	0.14	0.16	0.16	0.16
	7.5	0.12	0.13	0.14	0.15	0.16	0.16
	5.0	0.13	0.14	0.15	0.15	0.16	0.15
[0.2, 0.35]	15.0	0.13	0.15	0.16	0.18	0.18	0.18
	10.0	0.14	0.15	0.16	0.18	0.18	0.17
	7.5	0.14	0.14	0.16	0.16		

Table C.1. Parameters associated with the line profiles displayed in Fig. 3. V_{exp} is given in km s^{-1} , N_{H} in cm^{-2} . EW_{in} and W_{in} are given in \AA .

Prop.	True	Source A			Source B			Source C		
		IGM+z	IGM-z	No IGM	IGM+z	IGM-z	No IGM	IGM+z	IGM-z	No IGM
$\log V_{\text{exp}}$	1.9	$1.85^{0.17}_{0.23}$	$1.81^{0.29}_{0.39}$	$1.4^{0.11}_{0.11}$	$1.78^{0.19}_{0.27}$	$1.62^{0.16}_{0.2}$	$1.61^{0.14}_{0.1}$	$1.75^{0.19}_{0.21}$	$1.62^{0.15}_{0.16}$	$1.52^{0.17}_{0.21}$
$\log N_{\text{H}}$	17.5	$17.91^{0.16}_{0.24}$	$18.11^{0.26}_{0.32}$	$19.01^{0.28}_{0.16}$	$18.05^{0.2}_{0.27}$	$18.08^{0.26}_{0.32}$	$18.46^{0.4}_{0.36}$	$18.26^{0.19}_{0.23}$	$18.18^{0.26}_{0.38}$	$18.29^{0.32}_{0.36}$
$\log \tau_{\text{a}}$	-1.7	$-2.05^{0.13}_{0.17}$	$-2.12^{0.23}_{0.31}$	$-1.98^{0.47}_{0.69}$	$-2.16^{0.28}_{0.2}$	$-2.24^{0.23}_{0.27}$	$-2.2^{0.28}_{0.32}$	$-2.13^{0.2}_{0.2}$	$-2.09^{0.27}_{0.23}$	$-2.14^{0.22}_{0.21}$
$\log EW_{\text{in}}$	1.7	$1.78^{0.19}_{0.15}$	$1.77^{0.19}_{0.18}$	$1.58^{0.12}_{0.13}$	$1.89^{0.19}_{0.12}$	$1.82^{0.24}_{0.18}$	$1.73^{0.17}_{0.19}$	$1.82^{0.19}_{0.13}$	$1.75^{0.25}_{0.22}$	$1.64^{0.22}_{0.22}$
$\log W_{\text{in}}$	-0.6	$-0.62^{0.07}_{0.1}$	$-0.6^{0.07}_{0.07}$	$-0.61^{0.05}_{0.07}$	$-0.56^{0.11}_{0.14}$	$-0.61^{0.13}_{0.13}$	$-0.64^{0.09}_{0.1}$	$-0.59^{0.13}_{0.18}$	$-0.64^{0.12}_{0.16}$	$-0.72^{0.12}_{0.16}$
$f_{\text{esc}}^{4\text{\AA}}$	0.75	$0.81^{0.09}_{0.07}$	$0.82^{0.17}_{0.12}$	-	$0.76^{0.1}_{0.07}$	$0.84^{0.16}_{0.14}$	-	$0.73^{0.12}_{0.09}$	$0.7^{0.19}_{0.17}$	-
Prop.	True	Source D			Source E			Source F		
		IGM+z	IGM-z	No IGM	IGM+z	IGM-z	No IGM	IGM+z	IGM-z	No IGM
$\log V_{\text{exp}}$	2.0	$1.77^{0.17}_{0.17}$	$1.86^{0.1}_{0.12}$	$1.86^{0.14}_{0.13}$	$1.7^{0.23}_{0.26}$	$1.87^{0.27}_{0.24}$	$2.06^{0.24}_{0.13}$	$1.93^{0.23}_{0.19}$	$1.94^{0.22}_{0.24}$	$2.05^{0.27}_{0.28}$
$\log N_{\text{H}}$	19.5	$19.95^{0.3}_{0.21}$	$19.77^{0.31}_{0.33}$	$19.74^{0.26}_{0.24}$	$19.74^{0.4}_{0.34}$	$19.56^{0.51}_{0.38}$	$19.27^{0.31}_{0.3}$	$19.16^{0.7}_{0.66}$	$18.86^{0.67}_{0.68}$	$18.96^{0.6}_{0.55}$
$\log \tau_{\text{a}}$	-3.75	$-2.52^{0.24}_{0.42}$	$-2.28^{0.44}_{0.61}$	$-2.02^{0.68}_{0.86}$	$-2.26^{0.32}_{0.32}$	$-2.33^{0.39}_{0.41}$	$-2.33^{0.27}_{0.36}$	$-2.07^{0.28}_{0.26}$	$-2.11^{0.36}_{0.34}$	$-2.23^{0.36}_{0.29}$
$\log EW_{\text{in}}$	1.6	$1.73^{0.14}_{0.12}$	$1.74^{0.1}_{0.13}$	$1.71^{0.09}_{0.1}$	$1.58^{0.12}_{0.15}$	$1.62^{0.14}_{0.15}$	$1.58^{0.11}_{0.14}$	$1.81^{0.21}_{0.18}$	$1.77^{0.24}_{0.2}$	$1.72^{0.21}_{0.21}$
$\log W_{\text{in}}$	-0.1	$-0.22^{0.15}_{0.12}$	$-0.29^{0.15}_{0.16}$	$-0.23^{0.17}_{0.14}$	$-0.17^{0.17}_{0.16}$	$-0.24^{0.24}_{0.24}$	$-0.32^{0.18}_{0.22}$	$-0.26^{0.2}_{0.23}$	$-0.36^{0.22}_{0.33}$	$-0.34^{0.22}_{0.25}$
$f_{\text{esc}}^{4\text{\AA}}$	0.99	$0.94^{0.02}_{0.02}$	$0.95^{0.02}_{0.02}$	-	$0.88^{0.05}_{0.04}$	$0.9^{0.08}_{0.04}$	-	$0.78^{0.12}_{0.11}$	$0.81^{0.18}_{0.12}$	-
Prop.	True	Source G			Source H			Source I		
		IGM+z	IGM-z	No IGM	IGM+z	IGM-z	No IGM	IGM+z	IGM-z	No IGM
$\log V_{\text{exp}}$	2.4	$2.25^{0.07}_{0.08}$	$2.27^{0.18}_{0.14}$	$2.4^{0.14}_{0.11}$	$2.3^{0.24}_{0.21}$	$2.25^{0.27}_{0.45}$	$2.43^{0.27}_{0.26}$	$2.01^{0.3}_{0.34}$	$1.89^{0.27}_{0.3}$	$1.75^{0.53}_{0.6}$
$\log N_{\text{H}}$	18.4	$18.05^{0.27}_{0.31}$	$18.21^{0.44}_{0.42}$	$17.87^{0.27}_{0.43}$	$18.39^{0.48}_{0.7}$	$18.3^{0.71}_{0.75}$	$18.17^{0.55}_{0.93}$	$18.37^{0.52}_{0.85}$	$18.41^{0.76}_{1.21}$	$18.03^{0.48}_{0.97}$
$\log \tau_{\text{a}}$	-0.6	$-2.05^{0.46}_{0.37}$	$-2.1^{0.53}_{0.65}$	$-2.14^{0.43}_{0.49}$	$-2.08^{0.3}_{0.3}$	$-2.07^{0.39}_{0.42}$	$-1.93^{0.4}_{0.87}$	$-2.03^{0.26}_{0.22}$	$-2.11^{0.37}_{0.31}$	$-2.11^{0.31}_{0.31}$
$\log EW_{\text{in}}$	1.0	$1.0^{0.04}_{0.04}$	$1.01^{0.04}_{0.03}$	$0.92^{0.04}_{0.03}$	$1.06^{0.07}_{0.07}$	$1.06^{0.09}_{0.07}$	$0.98^{0.05}_{0.07}$	$1.32^{0.19}_{0.19}$	$1.33^{0.2}_{0.2}$	$1.2^{0.17}_{0.2}$
$\log W_{\text{in}}$	-0.8	$-0.63^{0.1}_{0.11}$	$-0.69^{0.12}_{0.1}$	$-0.62^{0.09}_{0.09}$	$-0.56^{0.14}_{0.16}$	$-0.65^{0.17}_{0.19}$	$-0.67^{0.1}_{0.12}$	$-0.47^{0.21}_{0.21}$	$-0.53^{0.17}_{0.19}$	$-0.63^{0.19}_{0.23}$
$f_{\text{esc}}^{4\text{\AA}}$	0.9	$0.82^{0.04}_{0.06}$	$0.88^{0.06}_{0.04}$	-	$0.76^{0.1}_{0.1}$	$0.81^{0.12}_{0.1}$	-	$0.67^{0.13}_{0.13}$	$0.78^{0.16}_{0.14}$	-

90% for many quality configurations. Also, we find that for $S/N_p > 7.5$ and $f_{\text{esc}}^{4\text{\AA}} > 0.5$ the $Q(KS = 0.1) > 70\%$ typically, even at $W_g = 4.0\text{\AA}$.

Notice that the outflow model confusion described in Sect. C is not the only contributor to $Q(KS = 0.1)$. The information destroyed by pixelization and noise affect $Q(KS = 0.1)$. For instance, $Q(KS = 0.1)$ for NoIGM, in the unabsorbed regime, goes from 98% in the best quality scenario down to 67% at the worst spectral quality.

Appendix E: Alternative models for $f_{\text{esc}}^{4\text{\AA}}$ inference

In this section we briefly discuss another model, REC+z. REC+z uses the recalibrated IGM transmission curves (as IGM-z) at the source redshift includes it in the input (as IGM+z). The redshift evolution in the $f_{\text{esc}}^{4\text{\AA}}$ distribution in shown in the left panel of

Fig. E.1. The REC+z model shows a similar $f_{\text{esc}}^{4\text{\AA}}$ distribution as IGM+z (see Fig. 5), however, at $z < 1.0$ the dispersion in REC+z is smaller, as 2σ of the sources have $f_{\text{esc}}^{4\text{\AA}} > 0.9$. In comparison, in IGM+z more than 2σ of the sources exhibit $f_{\text{esc}}^{4\text{\AA}} > 0.8$ at $z < 1.0$. The small variance at $z < 1.0$ in this training set is due to the fact that the IGM absorption at the $\text{Ly}\alpha$ wavelength is suppressed after the recalibration (see the right panel of Fig. 2).

The small scatter causes that REC+z $f_{\text{esc}}^{4\text{\AA}}$ measurements are biased towards high values at $z < 1.0$. This is shown in the right panel of Fig. E.1. Focusing in the mock 4 (grey), REC+z predicts a $\langle f_{\text{esc}}^{4\text{\AA}} \rangle$ about 0.9 when the true $\langle f_{\text{esc}}^{4\text{\AA}} \rangle$ is 0.8 at $z < 1.0$. Similarly, this is also clear in mock 3 (blue). The over prediction in REC+z at $z < 1.0$ is caused by the small $f_{\text{esc}}^{4\text{\AA}}$ scatter of the training set. As in the training set there is no source with $f_{\text{esc}}^{4\text{\AA}} \sim 0.8$ at $z < 1.0$,

$\sigma(\Delta\lambda_0[\text{\AA}]), z \in [0.0, 6.0]$							
f_{esc}	S/N _p	W_g	W_g	W_g	W_g	W_g	W_g
		0.1 \AA	0.25 \AA	0.5 \AA	1.0 \AA	2.0 \AA	4.0 \AA
[0.95, 1.0]	15.0	0.24	0.32	0.41	0.36	0.49	0.64
	10.0	0.39	0.34	0.41	0.55	0.62	0.88
	7.5	0.48	0.47	0.52	0.57	0.74	1.02
	5.0	0.48	0.56	0.66	0.99	1.08	1.59
[0.8, 0.95]	15.0	0.3	0.24	0.27	0.33	0.42	0.57
	10.0	0.28	0.31	0.32	0.41	0.54	0.77
	7.5	0.28	0.33	0.35	0.55	0.76	0.87
	5.0	0.38	0.45	0.72	0.7	0.86	1.82
[0.65, 0.8]	15.0	0.2	0.23	0.24	0.28	0.46	0.58
	10.0	0.23	0.24	0.27	0.36	0.49	1.18
	7.5	0.23	0.23	0.33	0.42	0.91	0.92
	5.0	0.34	0.4	0.41	0.55	1.52	1.57
[0.5, 0.65]	15.0	0.18	0.2	0.22	0.24	0.39	0.58
	10.0	0.17	0.25	0.23	0.31	0.47	1.12
	7.5	0.24	0.24	0.22	0.36	0.64	0.9
	5.0	0.23	0.29	0.32	0.86	1.34	2.15
[0.35, 0.5]	15.0	0.18	0.12	0.22	0.25	0.36	0.75
	10.0	0.21	0.19	0.22	0.35	0.51	1.13
	7.5	0.22	0.23	0.21	0.34	0.55	0.98
	5.0	0.18	0.32	0.51	1.08	1.91	2.34
[0.2, 0.35]	15.0	0.2	0.26	0.18	0.28	0.44	0.67
	10.0	0.45	0.28	0.66	0.4	0.37	1.37
	7.5	0.34	0.27	0.38	0.46	1.69	0.9
	5.0	0.45	0.36	0.84	1.09	0.94	2.13

$\sigma(\log V_{\text{exp}}[\text{km/s}], z \in [0.0, 6.0])$							
f_{esc}	S/N _p	W_g	W_g	W_g	W_g	W_g	W_g
		0.1 \AA	0.25 \AA	0.5 \AA	1.0 \AA	2.0 \AA	4.0 \AA
[0.95, 1.0]	15.0	0.14	0.17	0.2	0.26	0.34	0.44
	10.0	0.18	0.2	0.25	0.33	0.4	0.46
	7.5	0.2	0.25	0.28	0.37	0.43	0.48
	5.0	0.3	0.34	0.4	0.44	0.49	0.53
[0.8, 0.95]	15.0	0.19	0.18	0.2	0.3	0.35	0.43
	10.0	0.18	0.27	0.29	0.35	0.43	0.39
	7.5	0.24	0.28	0.32	0.38	0.41	0.48
	5.0	0.32	0.38	0.4	0.43	0.46	0.49
[0.65, 0.8]	15.0	0.23	0.29	0.33	0.45	0.45	0.49
	10.0	0.26	0.31	0.4	0.42	0.49	0.52
	7.5	0.33	0.4	0.42	0.51	0.48	0.56
	5.0	0.39	0.46	0.49	0.54	0.53	0.53
[0.5, 0.65]	15.0	0.35	0.35	0.4	0.47	0.53	0.55
	10.0	0.4	0.39	0.46	0.51	0.56	0.6
	7.5	0.39	0.47	0.48	0.56	0.56	0.56
	5.0	0.5	0.55	0.55	0.54	0.61	0.58
[0.35, 0.5]	15.0	0.46	0.51	0.47	0.52	0.63	0.63
	10.0	0.45	0.52	0.51	0.64	0.56	0.63
	7.5	0.55	0.56	0.62	0.64	0.57	0.66
	5.0	0.55	0.58	0.57	0.6	0.6	0.6
[0.2, 0.35]	15.0	0.56	0.53	0.58	0.52	0.55	0.52
	10.0	0.57	0.55	0.59	0.56	0.61	0.58
	7.5	0.58	0.65	0.51	0.49	0.64	0.69
	5.0	0.58	0.62	0.6	0.65	0.54	0.58

$\sigma(\log N_{\text{H}}[\text{cm}^{-2}]), z \in [0.0, 6.0]$							
f_{esc}	S/N _p	W_g	W_g	W_g	W_g	W_g	W_g
		0.1 \AA	0.25 \AA	0.5 \AA	1.0 \AA	2.0 \AA	4.0 \AA
[0.95, 1.0]	15.0	0.29	0.36	0.39	0.47	0.66	0.77
	10.0	0.32	0.4	0.52	0.65	0.7	0.87
	7.5	0.45	0.51	0.62	0.67	0.86	1.03
	5.0	0.56	0.63	0.79	0.83	0.98	1.16
[0.8, 0.95]	15.0	0.42	0.34	0.37	0.48	0.6	0.76
	10.0	0.37	0.43	0.49	0.56	0.75	0.88
	7.5	0.37	0.49	0.58	0.67	0.74	0.93
	5.0	0.53	0.6	0.74	0.78	0.92	0.99
[0.65, 0.8]	15.0	0.5	0.45	0.55	0.64	0.79	0.83
	10.0	0.54	0.56	0.63	0.67	0.8	0.95
	7.5	0.57	0.55	0.65	0.71	0.85	0.98
	5.0	0.55	0.69	0.71	0.82	0.87	1.09
[0.5, 0.65]	15.0	0.53	0.5	0.63	0.69	0.87	0.85
	10.0	0.57	0.59	0.73	0.76	0.78	1.0
	7.5	0.59	0.72	0.73	0.78	0.81	0.85
	5.0	0.61	0.72	0.71	0.78	0.93	1.03
[0.35, 0.5]	15.0	0.64	0.55	0.66	0.78	0.89	0.99
	10.0	0.57	0.67	0.74	0.85	0.89	0.91
	7.5	0.76	0.65	0.74	0.81	0.96	0.87
	5.0	0.69	0.73	0.7	0.81	0.79	0.71
[0.2, 0.35]	15.0	0.66	0.6	0.69	0.76	0.99	1.01
	10.0	0.66	0.59	0.85	0.76	0.95	0.85
	7.5	0.69	0.84	0.76	0.8	0.79	0.84
	5.0	0.69	0.76	0.76	0.78	0.66	1.04

$\sigma(\log EW_{\text{in}}[\text{\AA}]), z \in [0.0, 6.0]$							
f_{esc}	S/N _p	W_g	W_g	W_g	W_g	W_g	W_g
		0.1 \AA	0.25 \AA	0.5 \AA	1.0 \AA	2.0 \AA	4.0 \AA
[0.95, 1.0]	15.0	0.11	0.12	0.13	0.15	0.16	0.18
	10.0	0.12	0.13	0.14	0.17	0.18	0.2
	7.5	0.13	0.15	0.17	0.19	0.2	0.25
	5.0	0.18	0.19	0.2	0.23	0.26	0.29
[0.8, 0.95]	15.0	0.12	0.14	0.13	0.16	0.15	0.18
	10.0	0.14	0.15	0.17	0.17	0.18	0.21
	7.5	0.14	0.17	0.18	0.2	0.22	0.24
	5.0	0.17	0.19	0.21	0.24	0.29	0.28
[0.65, 0.8]	15.0	0.13	0.13	0.14	0.14	0.17	0.2
	10.0	0.14	0.15	0.15	0.17	0.19	0.21
	7.5	0.15	0.17	0.22	0.2	0.21	0.25
	5.0	0.19	0.2	0.22	0.24	0.25	0.28
[0.5, 0.65]	15.0	0.13	0.13	0.14	0.14	0.2	0.19
	10.0	0.11	0.12	0.16	0.15	0.2	0.19
	7.5	0.14	0.16	0.17	0.2	0.19	0.2
	5.0	0.18	0.18	0.18	0.2	0.25	0.26
[0.35, 0.5]	15.0	0.12	0.14	0.12	0.16	0.17	0.18
	10.0	0.11	0.12	0.16	0.17	0.17	0.24
	7.5	0.14	0.16	0.17	0.17	0.2	0.24
	5.0	0.18	0.18	0.18	0.2	0.22	0.26
[0.2, 0.35]	15.0	0.18	0.15	0.16	0.16	0.25	0.22
	10.0	0.22	0.19	0.17	0.19	0.23	0.21
	7.5	0.15	0.15	0.2	0.16	0.19	0.25
	5.0	0.13	0.17	0.2	0.21	0.22	0.24

$\sigma(\log W_{\text{in}}[\text{\AA}]), z \in [0.0, 6.0]$							
f_{esc}	S/N _p	W_g	W_g	W_g	W_g	W_g	W_g
		0.1 \AA	0.25 \AA	0.5 \AA	1.0 \AA	2.0 \AA	4.0 \AA
[0.95, 1.0]	15.0	0.23	0.25	0.26	0.3	0.32	0.37
	10.0	0.28	0.26	0.29	0.29	0.38	0.4
	7.5	0.28	0.3	0.32	0.36	0.36	0.42
	5.0	0.32	0.34	0.37	0.4	0.43	0.47
[0.8, 0.95]	15.0	0.28	0.27	0.3	0.33	0.35	0.39
	10.0	0.28	0.31	0.35	0.33	0.37	0.43
	7.5	0.31	0.33	0.34	0.38	0.39	0.43
	5.0	0.36	0.37	0.37	0.43	0.41	0.47
[0.65, 0.8]	15.0	0.28	0.27	0.26	0.27	0.37	0.38
	10.0	0.31	0.28	0.32	0.35	0.39	0.43
	7.5	0.3	0.29	0.34	0.37	0.38	0.43
	5.0	0.3	0.37	0.38	0.41	0.45	0.44
[0.5, 0.65]	15.0	0.21	0.22	0.25	0.29	0.3	0.34
	10.0	0.25	0.27	0.3	0.35	0.35	0.44
	7.5	0.26	0.27	0.31	0.36	0.37	0.45
	5.0	0.31	0.33	0.4	0.37	0.38	0.44
[0.35, 0.5]	15.0	0.17	0.16	0.28	0.28	0.33	0.41
	10.0	0.25	0.23	0.25	0.34	0.35	0.45
	7.5	0.23	0.29	0.27	0.32	0.36	0.42
	5.0	0.28	0.3	0.32	0.37	0.38	0.41
[0.2, 0.35]	15.0	0.25	0.39	0.16	0.37	0.37	0.42
	10.0	0.25	0.26	0.35	0.37	0.38	0.44
	7.5	0.28	0.26	0.33	0.32	0.4	0.42
	5.0	0.24	0.39	0.3	0.39	0.48	0.46

$\sigma(f_{\text{IGM}}^{\text{4A}}), z \in [0.0, 6.0]$							
f_{esc}	S/N _p	W_g	W_g	W_g	W_g	W_g	W_g
		0.1 \AA	0.25 \AA	0.5 \AA	1.0 \AA	2.0 \AA	4.0 \AA
[0.95, 1.0]	15.0	0.03	0.05	0.05	0.05	0.06	0.08
	10.0	0.03	0.03	0.06	0.07	0.08	0.09
	7.5	0.05	0.04	0.07	0.07	0.08	0.09
	5.0	0.04	0.05	0.07	0.08	0.11	0.1
[0.8, 0.95]	15.0	0.06	0.05	0.07	0.08	0.08	0.1
	10.0	0.05	0.06	0.07	0.08	0.1	0.1
	7.5	0.06	0.06	0.08	0.08	0.1	0.1
	5.0	0.06	0.06	0.08	0.1	0.11	0.11
[0.65, 0.8]	15.0	0.09	0.09	0.09	0.11	0.12	0.12
	10.0	0.09	0.1	0.1	0.12	0.13	0.13
	7.5	0.09	0.09	0.11	0.11	0.13	0.11
	5.0	0.08	0.09	0.09	0.12	0.11	0.12
[0.5, 0.65]	15.0	0.08	0.1	0.12	0.14	0.16	0.15
	10.0	0.09	0.1	0.12	0.14	0.16	0.14
	7.5	0.1	0.1	0.11	0.13	0.14	0.12
	5.0	0.09	0.1	0.09	0.12	0.14	0.13
[0.35, 0.5]	15.0	0.09	0.09	0.11	0.15	0.17	0.16
	10.0	0.1	0.09	0.12	0.14	0.16	0.15
	7.5	0.1	0.11	0.12	0.14	0.14	0.14
	5.0	0.08	0.09	0.11	0.11	0.15	0.13
[0.2, 0.35]	15.0	0.12	0.11	0.15	0.18	0.16	0.15
	10.0	0.14	0.13	0.15	0.16	0.17	0.16
	7.5	0.13	0.15	0.16	0.15	0.19	0.13
	5.0	0.1	0.11	0.1	0.14	0.15	0.14

$\sigma(\Delta\lambda_0[\text{\AA}]), z \in [0.0, 6.0]$							
f_{esc}	S/N _p	W_g	W_g	W_g	W_g	W_g	W_g
		0.1\AA	0.25\AA	0.5\AA	1.0\AA	2.0\AA	4.0\AA
[0.95, 1.0]	15.0	0.21	0.24	0.3	0.43	0.45	0.67
	10.0	0.31	0.28	0.33	0.46	0.58	1.02
	7.5	0.46	0.37	0.5	0.54	0.67	0.94
	5.0	0.41	0.5	0.66	0.94	1.04	1.56
[0.8, 0.95]	15.0	0.75	0.6	0.57	0.57	1.31	1.5
	10.0	0.57	0.53	0.58	1.16	0.64	0.93
	7.5	0.51	0.51	0.52	0.64	1.19	1.12
	5.0	0.53	0.59	1.08	0.8	0.91	1.9
[0.65, 0.8]	15.0	1.5	1.47	1.74	0.79	1.31	1.3
	10.0	0.96	1.1	0.73	1.51	1.23	2.3
	7.5	1.04	0.8	0.75	0.66	1.84	2.03
	5.0	0.76	1.29	0.92	1.11	1.98	2.29
[0.5, 0.65]	15.0	1.99	1.93	3.23	3.21	2.89	2.84
	10.0	2.3	1.35	1.68	2.24	2.63	2.4
	7.5	1.4	1.56	1.67	1.78	2.77	2.56
	5.0	1.0	1.65	1.93	1.91	2.47	3.09
[0.35, 0.5]	15.0	2.81	3.89	3.51	4.22	2.92	2.16
	10.0	2.98	1.56	2.29	1.88	2.57	2.3
	7.5	1.35	2.86	2.63	2.41	2.79	3.28
	5.0	1.51	2.49	2.6	3.03	3.57	3.5
[0.2, 0.35]	15.0	2.01	3.2	2.91	3.03	2.41	2.44
	10.0	2.36	3.3	3.07	2.75	3.37	3.32
	7.5	0.84	1.48	2.92	2.65	4.32	3.32
	5.0	0.85	2.29	2.79	3.55	3.85	3.69

$\sigma(\log V_{\text{exp}}[\text{km/s}], z \in [0.0, 6.0])$							
f_{esc}	S/N _p	W_g	W_g	W_g	W_g	W_g	W_g
		0.1\AA	0.25\AA	0.5\AA	1.0\AA	2.0\AA	4.0\AA
[0.95, 1.0]	15.0	0.11	0.12	0.15	0.19	0.28	0.35
	10.0	0.14	0.16	0.2	0.25	0.34	0.41
	7.5	0.15	0.2	0.23	0.29	0.37	0.43
	5.0	0.23	0.29	0.37	0.41	0.47	0.51
[0.8, 0.95]	15.0	0.35	0.4	0.34	0.39	0.39	0.4
	10.0	0.39	0.41	0.38	0.39	0.43	0.41
	7.5	0.33	0.37	0.36	0.41	0.41	0.45
	5.0	0.4	0.43	0.44	0.45	0.46	0.49
[0.65, 0.8]	15.0	0.64	0.7	0.58	0.66	0.6	0.58
	10.0	0.61	0.61	0.67	0.59	0.59	0.57
	7.5	0.66	0.6	0.63	0.67	0.56	0.59
	5.0	0.6	0.62	0.56	0.6	0.57	0.54
[0.5, 0.65]	15.0	0.64	0.61	0.67	0.63	0.56	0.67
	10.0	0.68	0.6	0.64	0.69	0.65	0.64
	7.5	0.62	0.72	0.64	0.69	0.6	0.6
	5.0	0.65	0.66	0.68	0.56	0.63	0.61
[0.35, 0.5]	15.0	0.71	0.74	0.67	0.72	0.69	0.62
	10.0	0.66	0.72	0.65	0.69	0.64	0.64
	7.5	0.64	0.66	0.76	0.74	0.63	0.68
	5.0	0.61	0.63	0.61	0.63	0.62	0.62
[0.2, 0.35]	15.0	0.79	0.71	0.85	0.63	0.64	0.65
	10.0	0.7	0.83	0.76	0.67	0.67	0.62
	7.5	0.81	0.8	0.77	0.66	0.74	0.71
	5.0	0.68	0.75	0.68	0.69	0.61	0.64

$\sigma(\log N_{\text{H}}[\text{cm}^{-2}], z \in [0.0, 6.0])$							
f_{esc}	S/N _p	W_g	W_g	W_g	W_g	W_g	W_g
		0.1\AA	0.25\AA	0.5\AA	1.0\AA	2.0\AA	4.0\AA
[0.95, 1.0]	15.0	0.21	0.28	0.31	0.38	0.56	0.68
	10.0	0.29	0.34	0.46	0.54	0.62	0.75
	7.5	0.35	0.42	0.53	0.62	0.81	0.94
	5.0	0.49	0.55	0.74	0.84	0.96	1.1
[0.8, 0.95]	15.0	0.63	0.51	0.53	0.67	0.67	0.81
	10.0	0.6	0.61	0.62	0.63	0.78	0.92
	7.5	0.54	0.61	0.62	0.71	0.81	0.9
	5.0	0.66	0.66	0.84	0.88	0.92	0.97
[0.65, 0.8]	15.0	0.89	0.73	0.96	0.94	0.99	1.01
	10.0	0.94	0.89	0.87	0.99	0.92	1.0
	7.5	0.97	0.87	0.92	0.95	0.99	1.08
	5.0	0.94	0.91	0.88	0.96	0.97	1.14
[0.5, 0.65]	15.0	1.01	0.92	1.16	0.95	1.07	1.16
	10.0	0.98	0.94	0.98	1.07	1.1	1.22
	7.5	0.98	1.05	0.94	1.06	0.98	1.05
	5.0	0.83	1.01	0.97	0.88	0.99	1.05
[0.35, 0.5]	15.0	1.08	1.13	1.1	0.94	1.14	1.21
	10.0	1.16	0.95	1.17	1.13	1.04	1.17
	7.5	1.14	1.03	1.14	0.98	1.13	1.07
	5.0	1.15	1.02	0.89	1.04	0.94	0.79
[0.2, 0.35]	15.0	0.94	1.11	1.08	1.12	1.06	1.09
	10.0	1.12	1.11	1.17	0.97	1.23	1.0
	7.5	1.23	1.09	1.16	1.04	0.84	0.99
	5.0	0.94	1.02	0.98	0.93	0.89	1.07

$\sigma(\log EW_{\text{in}}[\text{\AA}]), z \in [0.0, 6.0]$							
f_{esc}	S/N _p	W_g	W_g	W_g	W_g	W_g	W_g
		0.1\AA	0.25\AA	0.5\AA	1.0\AA	2.0\AA	4.0\AA
[0.95, 1.0]	15.0	0.11	0.11	0.12	0.13	0.15	0.15
	10.0	0.12	0.12	0.13	0.17	0.17	0.2
	7.5	0.13	0.14	0.16	0.18	0.2	0.23
	5.0	0.17	0.18	0.19	0.23	0.25	0.27
[0.8, 0.95]	15.0	0.33	0.29	0.3	0.31	0.26	0.27
	10.0	0.27	0.31	0.32	0.3	0.24	0.28
	7.5	0.3	0.29	0.3	0.27	0.29	0.27
	5.0	0.3	0.29	0.31	0.34	0.32	0.3
[0.65, 0.8]	15.0	0.39	0.36	0.32	0.28	0.31	0.31
	10.0	0.41	0.38	0.33	0.36	0.32	0.31
	7.5	0.38	0.35	0.36	0.37	0.36	0.33
	5.0	0.38	0.36	0.36	0.34	0.32	0.31
[0.5, 0.65]	15.0	0.37	0.35	0.33	0.31	0.28	0.27
	10.0	0.36	0.32	0.33	0.32	0.32	0.23
	7.5	0.35	0.38	0.36	0.32	0.29	0.29
	5.0	0.38	0.36	0.28	0.3	0.31	0.29
[0.35, 0.5]	15.0	0.36	0.32	0.31	0.31	0.3	0.25
	10.0	0.37	0.34	0.36	0.3	0.26	0.27
	7.5	0.29	0.36	0.35	0.29	0.3	0.27
	5.0	0.34	0.28	0.3	0.29	0.26	0.27
[0.2, 0.35]	15.0	0.25	0.32	0.29	0.35	0.3	0.25
	10.0	0.29	0.29	0.24	0.37	0.33	0.23
	7.5	0.27	0.31	0.37	0.28	0.25	0.29
	5.0	0.22	0.28	0.28	0.28	0.29	0.3

$\sigma(\log W_{\text{in}}[\text{\AA}]), z \in [0.0, 6.0]$							
f_{esc}	S/N _p	W_g	W_g	W_g	W_g	W_g	W_g
		0.1\AA	0.25\AA	0.5\AA	1.0\AA	2.0\AA	4.0\AA
[0.95, 1.0]	15.0	0.21	0.23	0.25	0.27	0.3	0.35
	10.0	0.26	0.25	0.27	0.29	0.36	0.38
	7.5	0.26	0.28	0.3	0.34	0.35	0.39
	5.0	0.3	0.32	0.36	0.39	0.42	0.46
[0.8, 0.95]	15.0	0.35	0.36	0.35	0.35	0.36	0.37
	10.0	0.37	0.35	0.38	0.35	0.37	0.43
	7.5	0.35	0.35	0.38	0.38	0.38	0.42
	5.0	0.39	0.39	0.37	0.43	0.4	0.46
[0.65, 0.8]	15.0	0.46	0.45	0.4	0.42	0.46	0.42
	10.0	0.44	0.39	0.43	0.45	0.45	0.44
	7.5	0.43	0.43	0.43	0.46	0.4	0.44
	5.0	0.39	0.43	0.42	0.43	0.47	0.45
[0.5, 0.65]	15.0	0.46	0.45	0.49	0.52	0.42	0.43
	10.0	0.53	0.48	0.52	0.47	0.42	0.5
	7.5	0.45	0.43	0.44	0.49	0.43	0.47
	5.0	0.47	0.45	0.5	0.44	0.42	0.46
[0.35, 0.5]	15.0	0.4	0.41	0.52	0.46	0.45	0.51
	10.0	0.51	0.44	0.4	0.5	0.5	0.46
	7.5	0.44	0.48	0.41	0.51	0.48	0.45
	5.0	0.4	0.45	0.42	0.47	0.42	0.41
[0.2, 0.35]	15.0	0.39	0.53	0.33	0.54	0.47	0.55
	10.0	0.47	0.42	0.4	0.52	0.52	0.47
	7.5	0.43	0.37	0.49	0.4	0.47	0.45
	5.0	0.42	0.52	0.39	0.45	0.49	0.47

Fig. C.3. Same as Fig. C.1 but for NoIGM.

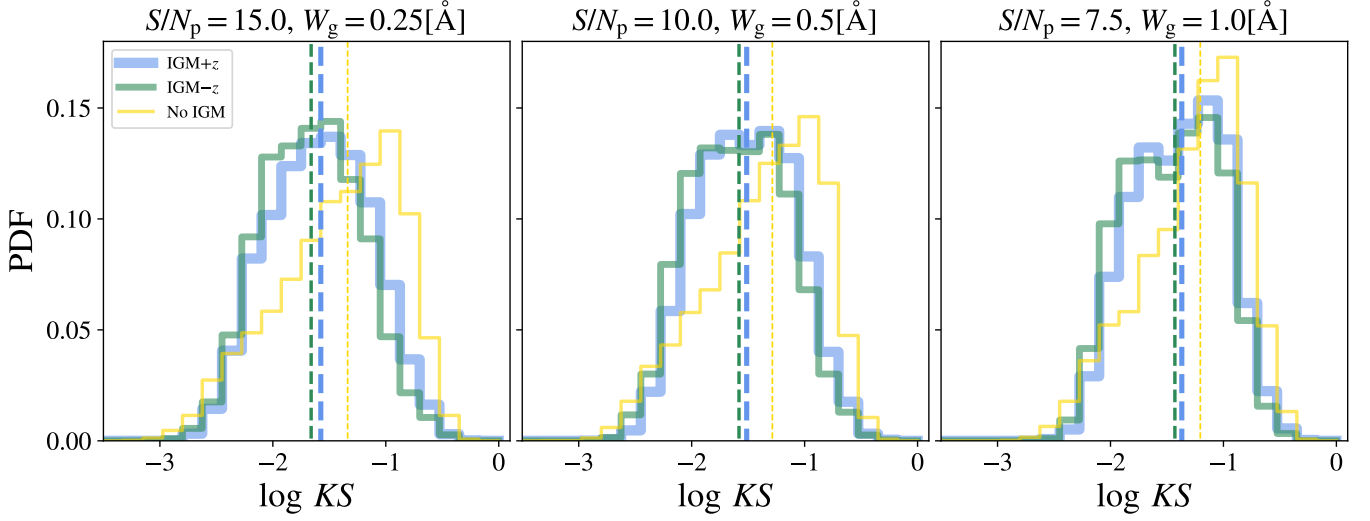


Fig. D.1. Kolmogórov-Smirnov estimator distribution comparison between models. zELDA's prediction using the IGM+z, IGM-z and NoIGM models are displayed in blue, green and yellow, respectively. Each subpanel show the KS distribution at different observed line profile qualities. In particular, in the left panel $S/N_p = 15.0$ and $W_g = 0.25\text{\AA}$, in the middle panel $S/N_p = 10.0$ and $W_g = 0.5\text{\AA}$, in the right panel $S/N_p = 7.0$ and $W_g = 1.0\text{\AA}$. The vertical dashed lines mark the median of the KS distribution of the matching color.

$\sigma(KS), z \in [0.0, 6.0]$							
f_{esc}	S/N_p	W_g 0.1 \AA	W_g 0.25 \AA	W_g 0.5 \AA	W_g 1.0 \AA	W_g 2.0 \AA	W_g 4.0 \AA
[0.95, 1.0]	15.0	0.03	0.03	0.03	0.03	0.04	0.06
	10.0	0.03	0.03	0.03	0.04	0.05	0.06
	7.5	0.03	0.03	0.04	0.04	0.05	0.07
	5.0	0.04	0.04	0.05	0.06	0.07	0.08
[0.8, 0.95]	15.0	0.03	0.03	0.03	0.03	0.03	0.05
	10.0	0.03	0.03	0.03	0.04	0.04	0.06
	7.5	0.03	0.03	0.03	0.04	0.05	0.06
	5.0	0.03	0.04	0.04	0.05	0.06	0.07
[0.65, 0.8]	15.0	0.03	0.03	0.03	0.03	0.04	0.04
	10.0	0.03	0.03	0.03	0.03	0.04	0.05
	7.5	0.03	0.03	0.04	0.04	0.05	0.05
	5.0	0.04	0.04	0.04	0.05	0.06	0.06
[0.5, 0.65]	15.0	0.03	0.03	0.03	0.04	0.04	0.05
	10.0	0.03	0.03	0.03	0.04	0.04	0.05
	7.5	0.03	0.03	0.04	0.04	0.05	0.05
	5.0	0.04	0.04	0.04	0.04	0.05	0.06
[0.35, 0.5]	15.0	0.04	0.04	0.04	0.04	0.05	0.05
	10.0	0.04	0.04	0.04	0.04	0.05	0.05
	7.5	0.04	0.04	0.04	0.05	0.05	0.06
	5.0	0.04	0.04	0.05	0.05	0.05	0.07
[0.2, 0.35]	15.0	0.06	0.06	0.06	0.06	0.06	0.06
	10.0	0.06	0.06	0.06	0.06	0.06	0.06
	7.5	0.06	0.06	0.07	0.06	0.07	0.08
	5.0	0.07	0.06	0.07	0.06	0.06	0.08

$Q_{50}(KS), z \in [0.0, 6.0]$							
f_{esc}	S/N_p	W_g 0.1 \AA	W_g 0.25 \AA	W_g 0.5 \AA	W_g 1.0 \AA	W_g 2.0 \AA	W_g 4.0 \AA
[0.95, 1.0]	15.0	0.02	0.02	0.02	0.02	0.03	0.04
	10.0	0.02	0.02	0.02	0.03	0.04	0.06
	7.5	0.02	0.02	0.03	0.03	0.05	0.07
	5.0	0.03	0.04	0.05	0.06	0.09	0.1
[0.8, 0.95]	15.0	0.02	0.02	0.02	0.03	0.03	0.04
	10.0	0.02	0.02	0.02	0.03	0.04	0.05
	7.5	0.02	0.03	0.03	0.04	0.05	0.07
	5.0	0.03	0.04	0.05	0.06	0.08	0.09
[0.65, 0.8]	15.0	0.02	0.02	0.02	0.03	0.03	0.04
	10.0	0.02	0.02	0.03	0.03	0.04	0.04
	7.5	0.03	0.03	0.03	0.04	0.04	0.06
	5.0	0.03	0.04	0.05	0.05	0.06	0.07
[0.5, 0.65]	15.0	0.02	0.02	0.02	0.03	0.04	0.04
	10.0	0.02	0.02	0.03	0.03	0.04	0.04
	7.5	0.03	0.03	0.03	0.03	0.04	0.05
	5.0	0.03	0.04	0.04	0.04	0.05	0.06
[0.35, 0.5]	15.0	0.03	0.03	0.03	0.04	0.04	0.05
	10.0	0.03	0.03	0.03	0.04	0.05	0.05
	7.5	0.03	0.03	0.03	0.04	0.05	0.05
	5.0	0.04	0.04	0.04	0.05	0.05	0.06
[0.2, 0.35]	15.0	0.06	0.05	0.06	0.08	0.07	0.07
	10.0	0.07	0.07	0.06	0.07	0.07	0.08
	7.5	0.06	0.07	0.06	0.07	0.08	0.08
	5.0	0.07	0.07	0.07	0.07	0.08	0.08

$Q_{50}(KS), z \in [0.0, 6.0]$							
f_{esc}	S/N_p	W_g 0.1 \AA	W_g 0.25 \AA	W_g 0.5 \AA	W_g 1.0 \AA	W_g 2.0 \AA	W_g 4.0 \AA
[0.95, 1.0]	15.0	0.01	0.01	0.01	0.02	0.02	0.03
	10.0	0.02	0.02	0.02	0.02	0.03	0.04
	7.5	0.02	0.02	0.02	0.03	0.04	0.05
	5.0	0.03	0.03	0.04	0.05	0.06	0.07
[0.8, 0.95]	15.0	0.04	0.04	0.04	0.04	0.05	0.05
	10.0	0.04	0.04	0.04	0.05	0.05	0.06
	7.5	0.04	0.04	0.04	0.05	0.06	0.07
	5.0	0.05	0.05	0.06	0.06	0.07	0.08
[0.65, 0.8]	15.0	0.07	0.07	0.07	0.08	0.08	0.09
	10.0	0.08	0.07	0.07	0.08	0.09	0.09
	7.5	0.08	0.08	0.07	0.08	0.09	0.09
	5.0	0.08	0.08	0.07	0.08	0.08	0.09
[0.5, 0.65]	15.0	0.1	0.1	0.1	0.11	0.12	0.12
	10.0	0.1	0.1	0.1	0.11	0.12	0.12
	7.5	0.1	0.1	0.1	0.1	0.12	0.11
	5.0	0.1	0.1	0.1	0.1	0.1	0.1
[0.35, 0.5]	15.0	0.13	0.12	0.13	0.14	0.15	0.15
	10.0	0.13	0.13	0.13	0.14	0.15	0.15
	7.5	0.12	0.12	0.13	0.13	0.14	0.14
	5.0	0.12	0.12	0.11	0.12	0.12	0.12
[0.2, 0.35]	15.0	0.14	0.15	0.15	0.17	0.17	0.18
	10.0	0.15	0.15	0.16	0.15	0.17	0.18
	7.5	0.13	0.15	0.14	0.16	0.17	0.17
	5.0	0.14	0.14	0.15	0.14	0.16	0.14

Fig. D.2. Median of the Kolmogórov-Smirnov distribution comparison between observed line profiles quality configurations and zELDA's models. The IGM+z, IGM-z and NoIGM are shown from left to right. Lighter colors match smaller number and vice versa.

$Q(KS=0.1), z \in [0.0, 6.0]$							
f_{esc}	S/N _p	W_g	W_g	W_g	W_g	W_g	W_g
		0.1Å	0.25Å	0.5Å	1.0Å	2.0Å	4.0Å
[0.95, 1.0]	15.0	96	97	97	96	89	77
	10.0	97	97	95	90	83	71
	7.5	97	94	89	84	74	65
	5.0	92	87	76	65	57	52
[0.8, 0.95]	15.0	98	97	97	97	93	84
	10.0	97	97	96	93	88	76
	7.5	97	96	94	89	80	69
	5.0	93	90	83	70	61	53
[0.65, 0.8]	15.0	97	96	95	95	90	86
	10.0	96	95	95	92	88	81
	7.5	95	94	92	87	81	74
	5.0	91	90	84	77	70	60
[0.5, 0.65]	15.0	96	95	95	93	91	87
	10.0	95	94	94	91	89	84
	7.5	95	93	93	89	81	78
	5.0	91	90	87	82	74	72
[0.35, 0.5]	15.0	93	92	91	91	86	83
	10.0	90	91	89	86	85	81
	7.5	89	90	85	86	81	78
	5.0	86	84	84	82	76	67
[0.2, 0.35]	15.0	76	74	77	70	71	73
	10.0	71	72	70	70	70	66
	7.5	65	72	64	70	63	62
	5.0	64	68	68	64	64	57

$Q(KS=0.1), z \in [0.0, 6.0]$							
f_{esc}	S/N _p	W_g	W_g	W_g	W_g	W_g	W_g
		0.1Å	0.25Å	0.5Å	1.0Å	2.0Å	4.0Å
[0.95, 1.0]	15.0	96	95	96	95	90	78
	10.0	94	95	94	92	83	69
	7.5	95	94	92	88	77	62
	5.0	93	88	80	70	57	49
[0.8, 0.95]	15.0	97	97	96	95	90	80
	10.0	96	95	95	92	85	73
	7.5	96	94	93	89	79	65
	5.0	92	88	81	72	60	52
[0.65, 0.8]	15.0	95	95	95	90	86	80
	10.0	94	94	93	88	84	77
	7.5	93	92	90	86	81	70
	5.0	89	87	82	77	68	61
[0.5, 0.65]	15.0	94	95	92	87	83	80
	10.0	94	93	91	85	81	78
	7.5	93	91	89	84	80	72
	5.0	90	86	83	79	73	65
[0.35, 0.5]	15.0	90	92	86	81	76	77
	10.0	90	87	82	79	72	72
	7.5	84	86	82	77	73	70
	5.0	80	78	79	75	72	67
[0.2, 0.35]	15.0	72	68	66	60	62	62
	10.0	68	65	65	61	64	59
	7.5	70	63	65	60	62	59
	5.0	61	62	60	65	57	59

$Q(KS=0.1), z \in [0.0, 6.0]$							
f_{esc}	S/N _p	W_g	W_g	W_g	W_g	W_g	W_g
		0.1Å	0.25Å	0.5Å	1.0Å	2.0Å	4.0Å
[0.95, 1.0]	15.0	98	98	98	97	95	92
	10.0	98	98	97	96	93	86
	7.5	98	96	96	93	87	81
	5.0	94	93	86	80	73	67
[0.8, 0.95]	15.0	85	86	84	83	80	79
	10.0	85	84	83	81	79	75
	7.5	83	85	82	79	76	70
	5.0	82	81	77	71	68	65
[0.65, 0.8]	15.0	62	66	62	62	58	54
	10.0	61	65	63	60	55	57
	7.5	62	63	64	61	59	55
	5.0	62	63	65	63	59	56
[0.5, 0.65]	15.0	50	51	48	41	38	38
	10.0	49	48	48	43	39	39
	7.5	50	49	47	46	39	42
	5.0	50	52	51	50	50	48
[0.35, 0.5]	15.0	32	36	32	26	24	23
	10.0	34	34	33	28	23	26
	7.5	35	38	36	33	30	33
	5.0	41	41	45	39	41	41
[0.2, 0.35]	15.0	29	26	24	14	20	18
	10.0	28	23	24	23	20	19
	7.5	32	30	25	26	22	25
	5.0	33	32	30	35	31	38

Fig. D.3. Percentile in the Kolmogórov-Smirnov distribution at which $KS=0.1$ for IGM+z, IGM-z and NoIGM are shown from left to right. Lighter colors match smaller number and vice versa.

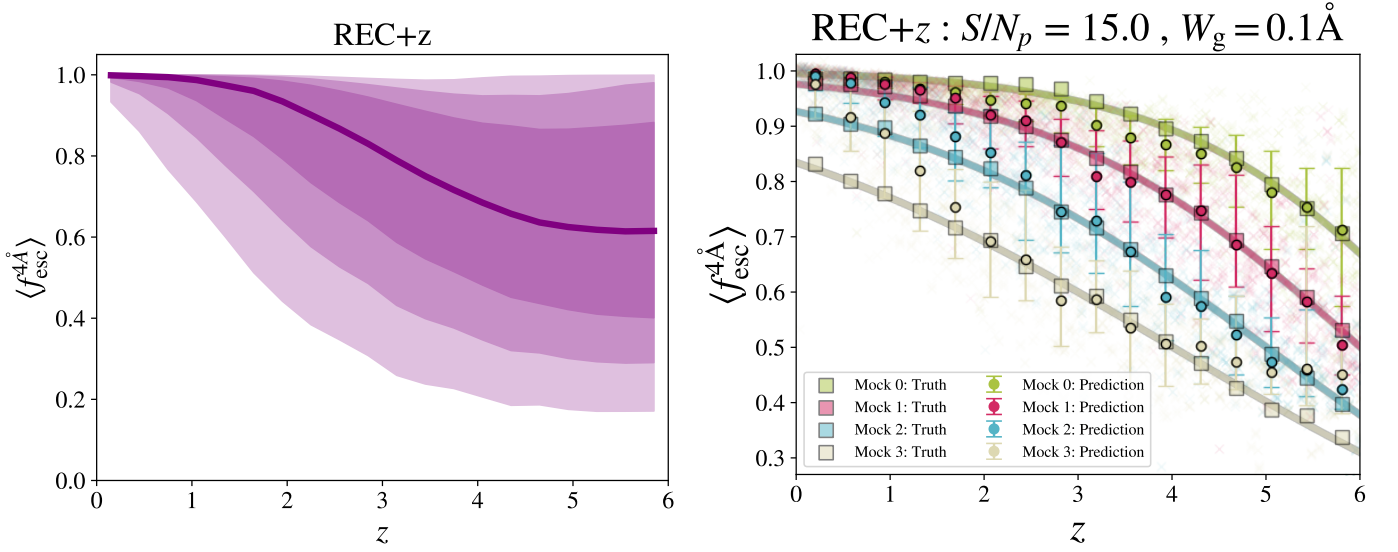


Fig. E.1. Left : $f_{\text{esc}}^{4\text{\AA}}$ distribution as a function of redshift in the REC+z model. The solid line shows the 50 percentile, while, from darker to lighter, the shadows show the 1σ , 2σ and 3σ . Right : Same as as Fig. 8 but for REC+z at $S/N_p=15.0$ and $W_{\text{in}}=0.1\text{\AA}$.